CHALMERS

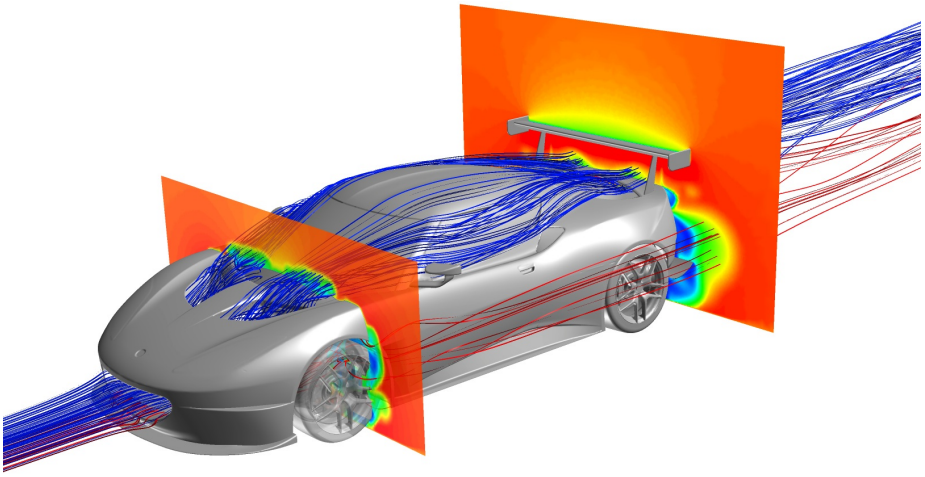

The Aerodynamic Influence of Rim Design on a Sports Car and its Interaction with the Wing and Diffuser Flow

Master's Thesis in Automotive Engineering

JOHAN CEDERLUND
JACOB VIKSTRÖM

Department of Applied Mechanics
Division of Vehicle Engineering and Autonomous Systems
CHALMERS UNIVERSITY OF TECHNOLOGY
Göteborg, Sweden 2010
Master's Thesis 2010:27

MASTER'S THESIS 2010:27

The Aerodynamic Influence of Rim Design on a Sports Car and its Interaction with the Wing and Diffuser Flow

Master's Thesis in Automotive Engineering

JOHAN CEDERLUND
JACOB VIKSTRÖM

Department of Applied Mechanics
Division of Vehicle Engineering and Autonomous Systems
CHALMERS UNIVERSITY OF TECHNOLOGY

Göteborg, Sweden 2010

The Aerodynamic Influence of Rim Design on a Sports Car and its Interaction with the Wing and Diffuser Flow
JOHAN CEDERLUND
JACOB VIKSTRÖM

Master's Thesis 2010:27
ISSN 1652-8557
Department of Applied Mechanics
Division of Vehicle Engineering and Autonomous Systems

Chalmers University of Technology
SE-412 96 Göteborg
Sweden
Telephone: + 46 (0)31-772 1000

Cover:
The Lotus Evora Type 124 Endurance Racecar with streamlines going through the cooling package and the brake cooling ducts and two coordinate planes showing the velocity magnitude.

Chalmers Reproservice
Göteborg, Sweden 2010

The Aerodynamic Influence of Rim Design on a Sports Car and its Interaction with the Wing and Diffuser Flow
Master's Thesis in Automotive Engineering
JOHAN CEDERLUND
JACOB VIKSTRÖM
Department of Applied Mechanics
Division of Vehicle Engineering and Autonomous Systems
Chalmers University of Technology

Abstract

Global climate change and increasing fuel prices demand more efficient vehicles. Today the automotive industry invests significantly into developing more efficient engines and to reduce the required force to propel the vehicles. For a passenger car the aerodynamic drag is a dominant part of the total resistance at highway speeds. In the area of sportscars, aerodynamic drag is even more dominant due to higher speeds and the fact that aerodynamics is also used in order to increase downforce. This result in contradictory demands as downforce often comes with a drag penalty. There has to be a delicate balance between the two. Even though the fuel price is not an issue when racing, there is a demand for efficient vehicles in order to obtain as much performance as possible within the rules.

The wheels have been shown to have a large influence on the global aerodynamic properties of a vehicle. It has also been shown that the local flow field around the wheels and wheel housings is highly dependent of the rim design.

In this project the influence on the global as well as the local aerodynamic properties from the rim design was studied. In addition the interaction between rim design and diffuser was investigated as well as the interaction between the diffuser and the wing.

The simulations showed clearly that a substantial decrease in drag can be achieved with proper rim design. Blocking the crossflow through the rims result in increased static pressure in the front wheel house and thereby an increase in lift, whereas blocking the crossflow in the rear result in increased downforce due to an increased flow rate through the diffuser. It was however shown that the resulting flow around the rear wheel was highly dependent of the rim design in the front. Furthermore it was shown that removing the lower wing increase the downforce generated from the upper wing whilst the base wake aft of the vehicle was substantially reduced and thus also the driving force for the diffuser leaving it less efficient.

Keywords: External Aerodynamics, Road Vehicle Aerodynamics, CFD, Wheel Modeling, Rim design, Drag Reduction, Downforce, Wing, Diffuser

Acknowledgement

We would like to thank our supervisors Dr. Lasse Malmkjær Christoffersen and David Söderblom at *Chalmers University of Technology* for all their help and advice. Special thanks to Christoffer Landström at *Chalmers University of Technology* that provided us with his expertise in wheel modeling and also some insight into the methods used for transient modelling. We would also like to thank our examiner Professor Lennart Löfdahl for giving us the opportunity to participate in such an interesting project.

We would also like to thank Louis Kerr at *Lotus Sport* for showing us their facilities as well as providing the geometry and his knowledge in the area of motorsports. We are also grateful to Ingemar Johansson at *Lotus Engineering* for his interest in our work and for the visit to the *Lotus Cars* factory.

Many thanks to Evangelos Skaperdas at *Beta CAE Systems* for his supervision and support in *ANSA*. Furthermore we are grateful to Peter Gullberg at *Chalmers University of Technology* for his software and hardware support.

Thanks to *Chalmers Computational Center of Sience and Engineering (C3SE)* for the opportunity to use their computational resources.

We would finally like to thank our families and friends for their support during our time at *Chalmers University of Technology.*

Nomenclature

a	Acceleration
A_f	Projected front area
C_D	Coefficient of drag
C_L	Coefficient of lift
F	Force
f_r	Rolling resistance coefficient
g_i	Gravitational acceleration
k	Turbulent kinetic energy
m	Mass
Ma	Mach number
N	Normal force
p	Static pressure
u^+	Dimensionless velocity
u^*	Friction velocity $u^* \equiv \sqrt{\frac{\tau_w}{\rho}}$
$\overline{u}$	Time averaged fluid velocity
U	Free stream velocity
u	Velocity
u'	Fluctuating part of fluid velocity
v	Velocity
w	Velocity
y^+	Dimensionless wall distance
α	Angle
ε	Dissipation
ℓ	Macroscopic turbulent length scale
ν	Kinematic viscosity
ρ	Density
τ_w	Wall shear stress
μ	Dynamic viscosity
ϑ	Macroscopic turbulent velocity scale

CAD	Computer Aided Design
CFD	Computational Fluid Dynamics
CFL	Courant-Friedrichs-Lewy condition (relation between flow velocity and timestep)
DNS	Direct Numerical Solution
LES	Large Eddy Simulation
MRF	Moving Reference Frame
NS	Navier Stokes
RANS	Reynolds Averaged Navier-Stokes
VCC	Volvo Car Corporation

Contents

1 Introduction

In this chapter the background, objectives, delimitations and methodology of this project in vehicle aerodynamics can be found.

1.1 Background

Due to the global climate change of today the automotive industry invests significantly in reducing the fuel consumption of their products. The companies are, at first hand, pushed by the governments and legislations to reduce the emissions of their vehicles. There are many aproaches to reduce the emissions and all of them are of importance for the automotive industry. One way is to switch to a more environmental friendly fuel or base the powertrain on other technologies such as electric or hybrid. A lot of work is put into making existing technology more efficient, for example reduction of internal friction, optimize combustion e.g. direct injection, spark timing etc, as well as downsizing and turbo charging of internal combustion engines. However one of the most effective aproaches is to reduce the driving resistance of the vehicle.

For a vehicle the following expression can be determined as the required force to propel the vehicle.

$$F_{req} = F_D + F_R + F_a + F_g \tag{1}$$

Where $F_D = \frac{1}{2} C_D \rho A_f v^2$ is the aerodynamic drag force, $F_R = N f_r$ is the force due to rolling resistance, $F_a = ma$ the force required to accelerate the vehicle and $F_g = mg \sin \alpha$ is the climbing resistance due to gravity [1].

The gravity and the inclination of the road can not be influenced by the designers and the acceleration is highly dependent on the behaviour of the driver. Hence the mass, the rolling resistance and the aerodynamics are the parameters left for the automotive industry to improve.

By plotting an approximation of the required force for steady state driving at 0° inclination as a function of velocity for a typical passenger car it can be noted that the different components of the resistance are of greater importance at different velocities [1], see Figure 1. This is a simplified and approximative plot to illustrate the magnitude of the forces for different velocities, of course the forces are highly dependent of the type of vehicle. Still in general for a typical passenger vehicle the rolling resistance and aerodynamic resistance are equal in around $60 km/h$ and at highway velocities the aerodynamic drag is the main source of driving resistance whereas the rolling resistance stays more or less constant.

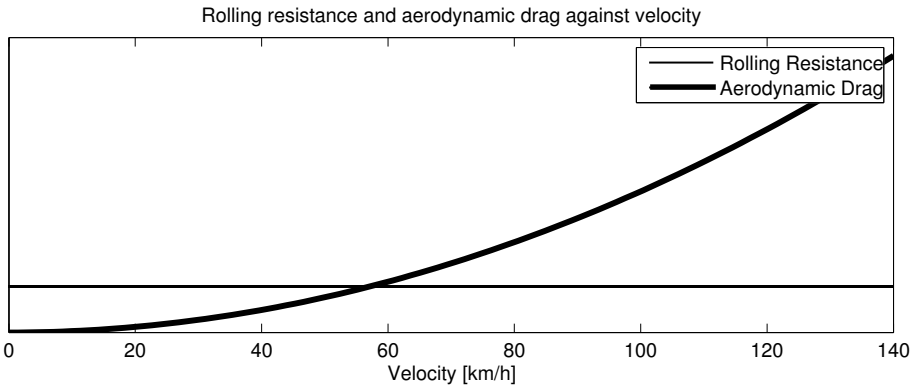

Figure 1: *Required force due to aerodynamic drag and rolling resistance as function of velocity*

For a racecar, generally operating in higher speeds, aerodynamic optimizations are of even greater importance. To improve the performance of a racecar a trade off between low aerodynamic drag and high downforce is necessary since conventional downforce generating devices increase the drag [1]. Due to regulations, the size and power of the engines of racecars are often limited and thereby the manufacturers are forced to make the most of the power available. The drag and lift must be balanced for each race depending on the current needs and obviously the downforce must be generated with as low drag penalty as possible.

The contribution, to the total aerodynamic drag, from the wheels is in the magnitude of 30% for an ordinary passenger car [2] and [3] and not much has happened in the field rim design as an effect of aerodynamic optimisation. A lot of the generated drag is an effect of the crossflow through the rims and thus there is large potential in decreasing the drag of the vehicle by optimising the rim design.

By increasing the coverage area of the rims the aerodynamic drag could be reduced as shown by Zhiling [4]. According to Dimitrou and Klussman [3] the downforce could be increased when the rims are enclosed. Thereby the effect on the flow field due to blockage of the crossflow through the rims is one of the main focuses in this study.

1.1.1 Researches in wheel aerodynamics

Fackrell and Harvey [5] and [6] showed the influence that an isolated rotating wheel had on the local flow field. They discovered a pressure peak above stagnation pressure in front of the contact patch that could only be explained by a jetting phenomena pushing the air to the sides of the wheel. Moreover they could conclude that the separation point at the top of the wheel was further forward than for a stationary wheel.

Mercker et al. [2] performed a large experiment with a number of different configurations. For example they measured the drag of the body without wheel, and compared the result with the drag for a complete vehicle with rotating wheels. The experiments showed that more than 30% of the total drag

is contributed from the wheels.

Axon et al. [7] showed that CFD can give reasonable good qualitative results for the flow around a wheel in their work where they compared experimental and numerical results for an isolated wheel.

Mears and Dominy [8] performed a similar investigation and found a good agreement between CFD and experiments in terms of drag. The jetting phenomena was also accurately predicted whereas the flow separation point and the lift forces were not adequately predicted.

McManus and Zhang [9] performed a numerical study of an isolated wheel and compared the results with the experimental results achieved from the work performed by Fackrell and Harvey [5]. The numerical solution predicted the surface pressure as well as drag and lift forces with a good accuracy overall. Allthough the agreement around the contact patch was found to be poor.

Dimitrou and Klussmann [3] performed a large investigation of wheel aerodynamics. They showed that open wheels gives a positive lift whereas enclosed wheels gives a significant amount of downforce as well as a reduction in drag.

Mlinaric [10] showed the importance of proper wheel modelling in CFD. A number of different configurations were carried out, including different wheel modelling techniques, different MRF-zones as well as different wheel designs. He showed that when using spoked rims, moving wall boundary condition provides an erroneous pressure distribution at spoke faces where the velocity is defined normal to the boundary. However using moving reference frame enveloping the critical surfaces of the spokes as a seperate cell zone and applying a rotational velocity of the fluid inside a more realistic result is achieved. Mlinaric also concludes that MRF shows good correlation for the flow fields around the wheel compared with, the more accurate but more computational demanding wheel rotation model, sliding mesh.

Landström [11] concluded from his work on rotating wheel modelling that numerical solutions, using MRF-zones, shows a good correlation with experimental results. Further the importance of correct wheel deformation is also identified by Landström.

Zhiling [4] performed a study on wheel aerodynamics in which he through experiments studied the influences from rim design and stationary rim shields. By designing a module-based prototype rim a large number of different setups could be tested by simply changing modules.

He concluded that covering the outer-radius part of the rim shows the largest potential to reduce drag. The wake area at the lower part of the wheel was shown to be significantly smaller for this rim due to blockage of crossflow through the rim. In general it was shown that the drag seemed to decrease with increasing covering area whereas the lift increased with incresing covering area. Changing rim shape details, spoke design, seemed to have little influence on the results.

1.2 Objectives

As mentioned before, the largest motivation for aerodynamic optimizations of today is to reduce the fuel consumption by decreasing the aerodynamic drag. However though this study is performed on a racecar where the increase of performance rather than lowering the fuel consumption is of interest. One has to remember that racecars are subjects of rigorous rules which require the manufacturers to optimise every aspect of the vehicle in order to utilise the power

supplied by the engine as efficiently as possible.

The work done by Zhiling [4] showed that the rim design is indeed a large source of drag and that it influences the global flow field. Through this study it is investigated if the conclusions from the work of Zhiling, also are applicable on a other car shapes, where for example the cooling outlets are positioned differently.

The main objectives for this study are to investigate how the rim design influence drag and lift forces and how it interacts with the diffuser and wings. It will consist both of evaluation of actual effects such as differences in drag and lift forces but also of evaluations of general effects on the flow fields around the parts of interest.

1.3 Delimitations

This study focus on the general aerodynamic properties of rims as well as how the rim design affects the local flow field around the wheel. Furthermore the influence on the diffuser from the rim design is investigated as well as the interactivity between the wing and the diffuser. The geometry used is the 2010, *Lotus Evora Type 124 Endurance Racecar*, supplied by *Lotus Sport*.

Only numerical methods are employed, thus no experimental measurements are carried out. However, different methods for modelling the rotation of the wheels are compared and evaluated. Simulations are performed at full and half vehicle geometries only, consequently no detail simulations of selected areas are performed. Time avaraged methods, RANS and unsteady RANS with realizable $k-\varepsilon$ as turbulence model, are used as solving methods. No transient solving methods e.g LES or DNS are used.

1.4 Methodology

In this study numerical simulations of different vehicle configurations are performed. Starting with evaluating the results of the baseline simulation, configurations of interest can be identified. For each configuration the CFD-process described below is performed. The CFD-process can be divided into three steps; pre-processing, solving and post-processing. Each step will be described individually below.

1.4.1 Pre-processing

The first step is to prepare the geometry for the simulation starting from a raw CAD-model. The CAD-model is cleaned up, reducing the level of detail, so that only surfaces of interest are left. Gaps that are too small to resolve that will not affect the result are filled in order to simplify the geometry. The CAD-cleanup was done using *ANSA* from *BETA CAE Systems.* An outer domain was then defined to set the outer dimensions of the virtual windtunnel.

The geometry is then covered with a surface mesh consisting of triangles in the magnitude of $3-10mm$ depending on the shape of the geometry. The mesh should represent the geometry as well as possible and the areas where the results are of higher interest should be in higher resolution. In order to resolve the flow close to the wall, a number of layers consisting of prisms generated from the triangles in the surface mesh.

The domain is then filled with volume cells of tetrahedron and heaxahedron types. In this phase it is benificial to have higher resolution in the areas of greater interest. The mesh generation is done using *ANSA* from *BETA CAE Systems* for surface mesh, layers and volume mesh.

1.4.2 Solving

In the solving step the computational mesh generated during the pre-processing is used to achieve the flow field parameters. The solver discritizes the time averaged NS-equations, RANS, completed with the realizable $k - \varepsilon$ turbulence model to solve for the velocities and pressure in each cell by iterating through the domain until convergence is reached. For each boundary of the domain a specified boundary condition is set e.g. inlet, outlet and walls. *Fluent 12.0* from *Ansys* is used as solver.

1.4.3 Post-processing

By extracting the physical quantities from the solver, the results can be visualized. The result can be displayed in a numerous of ways e.g. streamlines, iso-surfaces and color contour plots on defined coordinate planes or existing surfaces. The pressure and viscous forces on a part that has wall properties can be calculated from the results. For post-processing *Fluent 12.0* from *Ansys* is used to calculate forces and *FieldView* from *Intelligent Light* is used for the graphical post-processing.

2 Numeric simulations

The base of this study consists of numeric simulations, carried out using *Computational Fluid Dynamics* - CFD. CFD is a tool, designed to solve the governing equations of fluid flow using an iterative method for a finite number of cells, in other words, a finite number of points in the domain in which the state variables are determined.

2.1 Numerical methods

The governing equations for the time dependent three-dimensional fluid flow and heat transfer around a body are the continuity equation, momentum equations and energy equation [12]. The general approach in road vehicle external aerodynamics is to assume incompressible and isothermal flow [1], the flow can be considered incompressible when $Ma < 0.3$ [13], which is in the vicinity of $100m/s$ at sea-level and it is unlikely that the flow will reach this velocity anywhere in the domain. Thus the energy equation can be neglected and the momentum- and continuity equations can be written on incompressible form, neglecting the density terms [13].

The continuity equation is thus written

$$\frac{\partial u}{\partial x} + \frac{\partial v}{\partial y} + \frac{\partial w}{\partial z} = 0 \tag{2}$$

and the momentum equations.

$$\begin{aligned}
\rho g_x - \frac{\partial p}{\partial x} + \mu \left(\frac{\partial^2 u}{\partial x^2} + \frac{\partial^2 u}{\partial y^2} + \frac{\partial^2 u}{\partial z^2} \right) &= \rho \frac{du}{dt} \\
\rho g_y - \frac{\partial p}{\partial y} + \mu \left(\frac{\partial^2 v}{\partial x^2} + \frac{\partial^2 v}{\partial y^2} + \frac{\partial^2 v}{\partial z^2} \right) &= \rho \frac{dv}{dt} \\
\rho g_z - \frac{\partial p}{\partial z} + \mu \left(\frac{\partial^2 w}{\partial x^2} + \frac{\partial^2 w}{\partial y^2} + \frac{\partial^2 w}{\partial z^2} \right) &= \rho \frac{dw}{dt}
\end{aligned} \tag{3}$$

The momentum equations, 3, are normally referred to as the *Incompressible Flow Navier-Stokes equations* [13]. They are second order non-linear partial differential equations with only a few known analytical solutions. The main problem in solving the Navier-Stokes equations is that account has to be taken to the turbulence in order for the solution to match the physical flow accurately.

However, the equations are solved for a finite number of control-volumes which are usually referred to as a computational grid. According to Barnard [1] it has been estimated that the computational grid for the flow around a passenger vehicle if it were to resolve all turbulent scales would have to be around 10^{18} cells. Whereas the computational grids in this study are about $4 \cdot 10^7$. It will not be possible or practical yet for many years to use grids of the size mentioned by Barnard. Due to this fact there is a need to model these equations in order to obtain an approximate solution for coarser computational meshes.

2.1.1 RANS

The most common and simplest way to model the Navier Stokes equations is using what is often referred to as *the Reynolds Decomposition*. This approach consists of rewriting the terms in the equations as time-averaged terms. For example the time average of the turbulent function $u(x, y, z, t)$, which is the velocity in the x-direction.

$$\overline{u} = \frac{1}{T}\int_0^T u\, dt \tag{4}$$

The fluctuating term u' is defined as the deviation of u compared to the time averaged value

$$u' = u - \overline{u} \tag{5}$$

Thus all properties are split into mean and fluctuating parts.

$$\begin{aligned} u &= \overline{u} + u' \\ v &= \overline{v} + v' \\ w &= \overline{w} + w' \\ p &= \overline{p} + p' \end{aligned} \tag{6}$$

Substituting these into equations 3 and 2 and taking the time mean of each equation yields in the x-direction for the momentum equations

$$\begin{aligned} \rho\frac{d\overline{u}}{dt} &= -\frac{\partial\overline{p}}{\partial x} + \rho g_x + \frac{\partial}{\partial x}\left(\mu\frac{\partial\overline{u}}{\partial x} - \rho\overline{u'^2}\right) \\ &\quad + \frac{\partial}{\partial y}\left(\mu\frac{\partial\overline{u}}{\partial y} - \rho\overline{u'v'}\right) + \frac{\partial}{\partial z}\left(\mu\frac{\partial\overline{u}}{\partial z} - \rho\overline{u'w'}\right) \end{aligned} \tag{7}$$

The rewritten Navier-Stokes equations contains only time-averaged terms and fluctuating terms, the latter are normally referred to as *turbulent stresses.* This formulation is called *Reynolds Averaged Navier-Stokes*, abbreviated *RANS*.

The turbulent stresses cannot be solved analytically but requires modelling using turbulence models [12] this is often referred to as the *closure problem.*

2.1.2 Modelling turbulence

Turbulence modelling is done using many different approaches. One of the most common methods is using the *Eddy Viscosity model* where the turbulence is modeled by adding an additional viscosity, the *turbulent viscosity* μ_t [14].

In this study a variant of the $k-\varepsilon$-model has been used, the *realizable* $k-\varepsilon$*-model*. The $k-\varepsilon$-model is an eddy viscosity-, two equation model consisting of the transport equations for the turbulent kinetic energy, k, and the dissipation, ε. The k and the ε are used to define turbulent velocity and length scale, ϑ and ℓ [12]. In particular the *realizable* $k-\varepsilon$*-model* consists of a new transport equation for the dissipation rate, ε, which has been derived from an exact equation for the transport of the mean-square vorticity fluctuation, whereas the standard

$k-\varepsilon$*-model* consists of a transport equation for the dissipation rate, ε, which has been derived through physical reasoning and does not really resemble its exact counterpart [15]. It is supposed to generate far more accurate results for flows involving for example rotation and separation. [15]. The realizable $k-\varepsilon$-model is considered to generate good results in the field of external road vehicle aerodynamics according to, for example, VCC.

The realizible $k-\varepsilon$-model is used in combination with non-equilibrium wall functions, see section 2.1.3. The behaviour close to the wall is thus modelled using functions that are empirically created. It can be shown that the $k-\varepsilon$-model functions poorly close to the wall without the addition of wall functions or increased mesh resolution.

2.1.3 Wall functions

Since the $k-\varepsilon$-turbulence models are valid, primarily, at some distance from walls, wall-treatment is needed in order to accurately determine the flow in areas close to walls [16].

Due to the fact that the no-slip condition at walls need to be satisfied, the mean velocity field will be influenced [15]. However, the flow is influenced in more complex ways as well. Usually the region close to the wall is divided into three zones. Very close to the wall is, what is usually called, the *viscous sublayer* where viscous damping reduce the tangential velocity fluctuations and normal velocity fluctuations are reduced by kinematic blocking [15]. The flow in this region is thus almost laminar. After the viscous sublayer comes the, so called, *buffer layer* and the fully turbulent *log-law region,* see Figure *2.* Throughout these regions the turbulence is rapidly increased due to the increase in kinetic energy which is an effect of the large mean-velocity gradients.

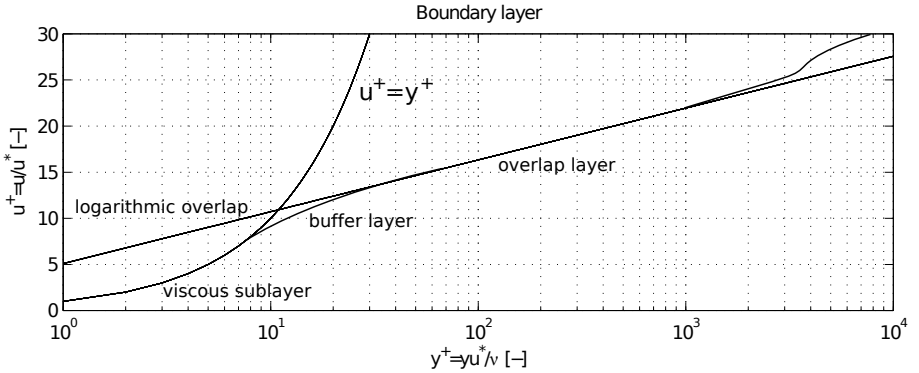

Figure 2: *A schematic of the velocity profile in a turbulent boundary layer.*

There are in principle two ways of handling this problem, one being to actually resolve the strong gradients in the boundary layer with a very fine mesh, the *near-wall model approach*, and the other is to assume that the flow near the wall behaves like a fully turbulent boundary layer and employ *wall functions* [17] the latter being the one used in this study. The wall function approach is less computational heavy and offer sufficient accuracy in most applications, but for, for example, applications where the flow is highly skewed or laminar the

near-wall model approach would be a better choice. The main practical difference between these two methods in the pre-processing phase is the fact that the centre of gravity for the first cell should be close to $y^+ = 1$ for the *near-wall model approach* and $30 \leq y^+ \leq 300$ for the *wall functions*. For more details about the aspect of meshing, see section 2.3.1.

Wall functions are semi-empirical functions derived from experiments and they consist of *laws of the wall* for the mean velocity and other scalars and known correlations for turbulent quantities close to the wall.

In particular the *non-equilibrium wall function* employed in this study also take into account the effect of pressure gradients on the distortion of velocity profiles. The assumption of local equilibrium is not valid in such cases, thus the non equilibrium effects neglected by standard wall functions are partly accounted for in the non. eq. wall functions [15].

2.2 Modelling wheel rotation

Conducting steady simulations on transient processes involves many modelling aspects, one of them being rotation of certain parts of the geometry. In particular, for vehicle aerodynamics, the rotation of wheels is a challenge. Depending on the nature of the geometry of the wheel and rim, different methods of modelling are required. The most common methods are described below.

2.2.1 Moving wall

The easiest and most straightforward way of modelling the rotation of the wheel and rim, is to introduce a rotational velocity as boundary condition on the surface, this is what in Fluent is called *moving wall*. However though, this requires that the rotating geometry does not have walls with rotational motion in the direction of the normal of the wall [16] such as the part of the spokes with normals in the x-direction. In other words, spoked rims cannot be accurately represented by this boundary condition and for example, one effect will be that the pressure increase and decrease on the inner and outer wall of each spoke will not be modelled. This has also been shown by Mlinaric [10].

2.2.2 MRF - Multiple reference frame

A more accurate method of accounting for the rotation of a geometry with motion normal to the walls is the MRF-method. It is together with the sliding mesh method one of the two approaches available in *Fluent* for multiple rotating cell zones.

The MRF-method is often referred to as the *frozen rotor approach* this obviously due to the fact that the method does not account for actual movement of the geometry. Thus it is not suitable in applications where large gradients can appear due to interaction between the inertial reference frame and the rotating reference frame, such as in turbo machinery with strong interaction between rotor and stator. As long as the flow is relatively uncomplicated in the interface zone between the rotating and stationary zone the MRF-method usually generates good results.

When solving the equations of motion, using the MRF-approach, the acceleration of the fluid is increased by additional terms in the momentum equations

[15] and thus forces due to the relative motion of the spokes is accounted for.

A good correlation between MRF-, sliding mesh and experiments have been proven by Mlinaric [10]. A comparison between the wheel modeling methods, MRF and moving wall, is found in Appendix C.

However special attention needs to be put on the aspect of meshing when using the MRF-method, see section 2.3.2.

2.2.3 Sliding mesh

The sliding mesh method accounts for the relative motion of rotating and stationary parts and the unsteady interactions that follow. It is the most accurate method for simulating flows in multiple rotating reference frames but due to the fact that the mesh needs to be updated and that the method, of course, require transient simulations it is also the most computational demanding method.

As well as for the MRF-method certain attention needs to be put on the aspect of meshing, for example the interface zone needs to be completely cylindrical in order to ensure that there is contact in the interface zone at all times, see section 2.3.2. There are very different requirements for the mesh close to the rims depending on which method that is chosen to model the rotation.

2.3 Numerical setup

The geometry used in the simulations is the *Lotus Evora Type 124 Endurance Racecar*. It is a highly detailed model and has only been slightly simplified in order to make it suitable for CFD-simulations. The largest difference from the original geometry is the lack of engine bay and engine. But since the engine is mounted in the rear it will not significantly influence the flow around the wheels and is considered to be a fair simplification to the model. Other than that only gaps and small features $\sim 3mm$ have been removed or approximated. The cooling duct in the front together with radiator is fully detailed except for the casing for the fans. And since this is a race car there is no condenser in the cooling package as it would have been on a normal passenger vehicle.

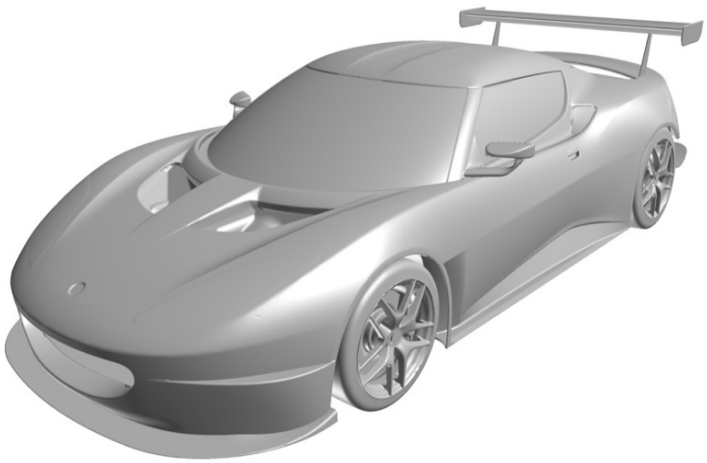

Figure 3: *The vehicle geometry used in the study*

As previously mentioned, the geometry was cleaned, prepared and surface- as well as volume-meshed in the commercial software *ANSA* from *BETA CAE Systems.* The solver used for all simulations is the commercial CFD-code *Ansys Fluent 12.0.* Post processing has been done, mainly using *Intelligent Light Fieldview* together with the post processor in *Fluent 12.0.*

2.3.1 Computational grid

The computational domain is based on the current practice for external aerodynamics, it is created as a rectangular wind tunnel test section. It is approximatley 2 vehicle lengths upstream the vehicle and 8 vehicle lengths downstrem. The test section is around 5 vehicle widths wide and around 5 vehicle heights high. That gives a test section with the outer dimensions, 10 meters wide, 50 meters long and a height of 6 meters. The computational domain can be seen in Figure 4. The origin of the coordinate system, $(0, 0, 0)$ is located at ground level, in the symmetry plane of the vehicle and at $216mm$ downstream the front most point of the vehicle.

The surface mesh of the vehicle is created as a representation of the geometry with a finite number of elements. Using the surface mesh of the vehicle and the surface mesh of the windtunnel geometry a closed volume is created in which cells can be grown. In every cell the physical quantities of the flow is later determined by the solver.

The surface mesh of the vehicle has a resolution, or rather cell size of between 3 to $10mm$. The main focus and the highest resolution is of course in the vicinity of the wheels, wing and diffuser since this is the main areas of interest in the study.

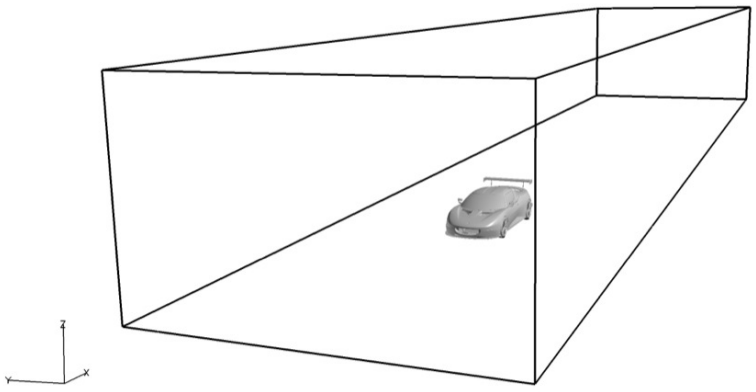

Figure 4: *The computational domain*

Since the velocity at a wall is zero and due to the fact that it will increase quite rapidly and somewhat irregularly over a small distance $\sim 0 < y^+ < 300$, in the area where wall functions are ususally utilized, see section 2.1.3, in order to predict the flow accurately, there is a need for smaller cells in this area. Ideally each wall-adjecent cell's centre of gravity should be located within the log-law layer which is in the region $30 < y^+ < 300$, however, it is desireable to have it located closer to the lower bound.

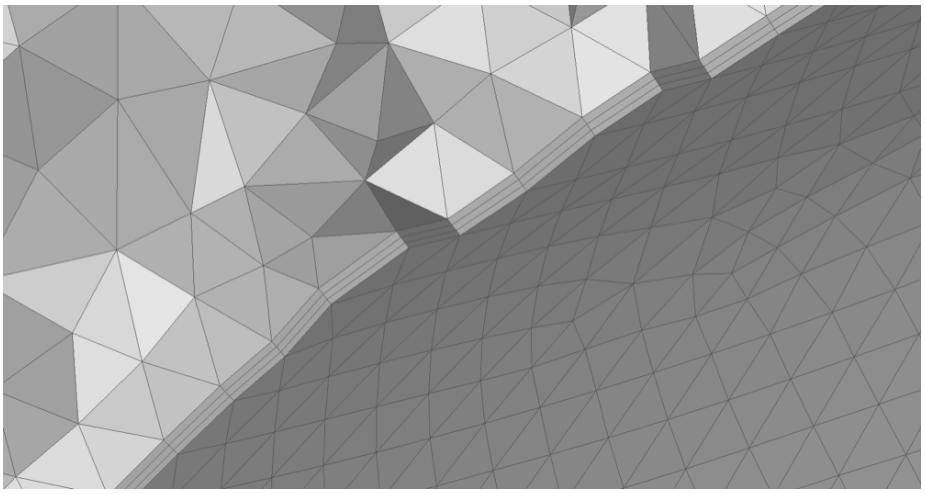

Figure 5: *A close-up of the prism layers close to the walls of the vehicle*

This is usually solved by creating layers of thin prism cells close to the wall, see Figure 5. Prism cells enable the possibility of creating thin but wide cells

which are ideal in areas close to walls. In this particular application the first cell height is estimated, through equation 8 and 9, to $0.9mm$ in order to obtain a y^+ value for the first cell in the vicinity of 100. The following two cells are grown with a geometric growth rate of 1.1.

$$y = \frac{\nu y^+}{u^*} \tag{8}$$

where

$$u^* \approx 0,05U \tag{9}$$

Regarding the wind tunnel domain it is divided into two, one inner domain which is close to the vehicle in which tetrahedron-cells are grown and one large outer domain in which a hexa-dominant mesh is grown. The actual meshing process in the inner domain is to a large extent controlled by mesh-refinement zones which can be seen in Figure 6.

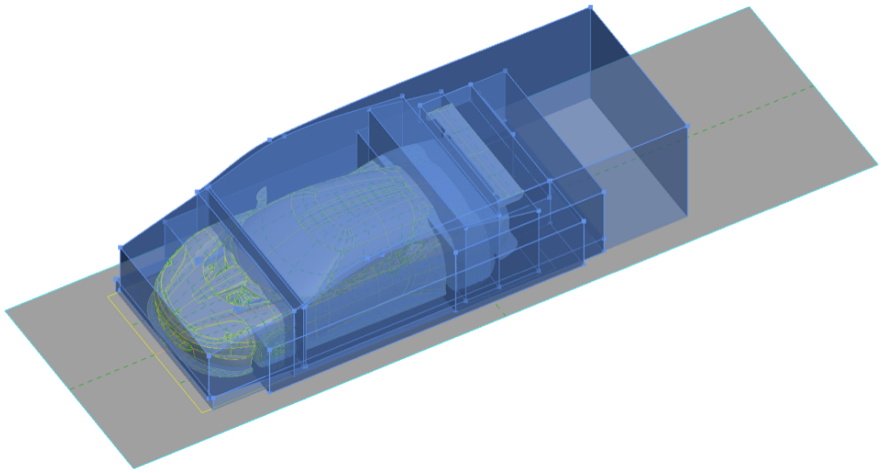

Figure 6: *The Refinement zones used when generating the volume mesh*

The refinement zones are mainly situated around the wheels, wheelhouses, wing and diffuser where the cell size is limited to $10mm$. The refinement zones are also controlling several other stages of zones of specified resolution in the base wake area as well as close to the floor and underbody of the vehicle. The zones range from 10 to $40mm$.

The resulting mesh consists of an inner domain with close to 40 million tetrahedra and an outer domain of a combination of 0.33 million hex and tetrahedra. The meshes have a maximum skewness of 0.97 with a mere 400 cells above 0.9.

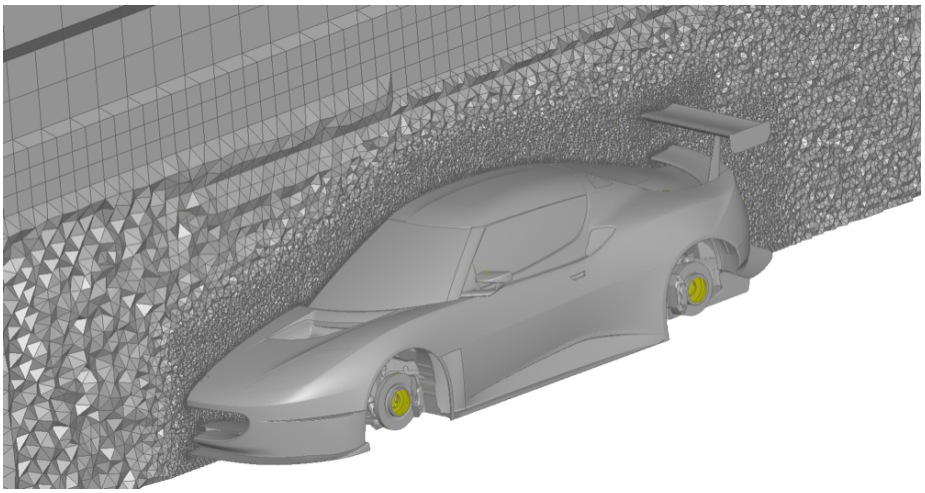

Figure 7: *A cross section cut of the volume mesh in the center of the domain.*

A cross section cut of the mesh can be seen in Figure 7. The influence of the refinement zones and the transition to hex-cells are clearly visible.

2.3.2 Computational grid close to the wheels

Certain attention has to be put into the meshing of the volume close to the wheels when using methods such as MRF or sliding mesh, see section 2.2. In this particular study, two different set-ups have been used, one in the MRF-simulations and one in the sliding mesh simulation.

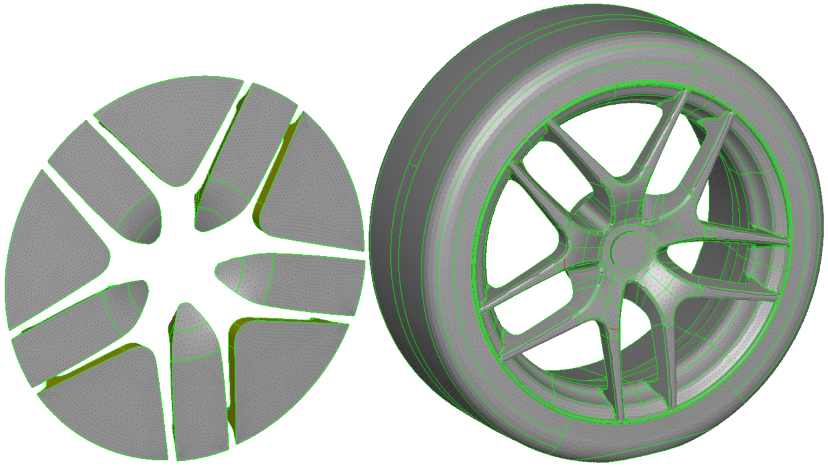

Figure 8: *The MRF-fluid zones are visible to the left and the wheel and rim to the right*

In accordance with [10] the MRF-zones are created like cake pieces, encapsulating the fluid between the spokes of the rim, see Figure 8. This is what Mlinaric [10] refers to as the *"Practical MRF region"* which has proven to generate good results.

The mesh in these zones is limited to a cell size of maximum $10mm$.

One of the main concerns when designing a MRF-region is to make sure the region is not extending into the flow field which is dominated by high velocity translatory flow that is passing the side of the vehicle. This is due to the fact that the translatory flow is not considered uniform in the reference frame if it is perpendicular to the axis of rotation.

On the other hand, when designing a cell zone for *Sliding Mesh* simulations the main concern is to create a simple interface zone between the rotating cell zone and the stationary cell zone. The common practice is to create a cylindrical zone which is an extension of the rim, see Figure 9.

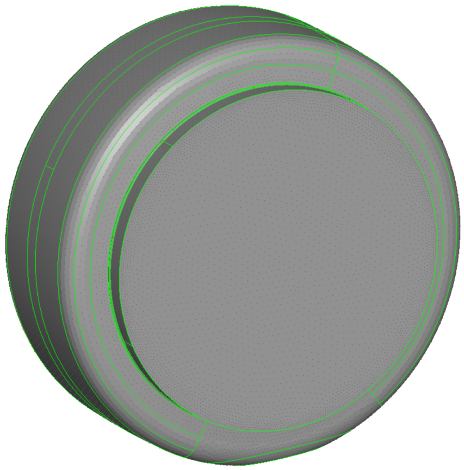

Figure 9: *The front wheel with the extended cylinder which encapsulates the cell zone which is rotating when using sliding mesh to model wheel rotation.*

The interface need to be completely symmetric and cylindrical to ensure contact in the interface during the rotation of the wheel [16]. Obviously the interface zone could be meshed in such a manor that there would be conformal interfaces as the wheel rotates. However though the workload in creating such a mesh is considered to be too large in comparison to the small workload and the good results that can be obtained using non-conformal interfaces and a standard surface mesh.

2.3.3 Solver set-up

The solver set-up is of course a section in which a lot can be written, but this section will only cover certain, vital, parts of the solver set-up. The solver used is, as previously mentioned, the *Fluent 12.0* package.

In accordance with the current knowledge and practice in the automotive industry all simulations run in this study have been solved using *RANS* and the realizable $k-\varepsilon$-turbulence model together with non-equilibrium wall functions.

The flow can be assumed to be incompressible when $Ma < 0.3$ [13], which is approximately $100m/s$ at sea level. It is not likely that a velocity above that is achieved at any place in the domain when the inlet condition is set to $38.89m/s$, hence the flow can be considered incompressible.

In order to model the relative velocity of the windtunnel floor, the boundary condition is set to *moving wall* with a translational velocity of $38.89 m/s$ which is the free stream velocity, the boundary condition on the other artificial windtunnel walls are set to *symmetry*, which is a wall without *no-slip condition*.

The inlet is set to *velocity inlet* with an absolute flow velocity of $38.89 m/s$ normal to the boundary, which is a standard test speed in the automotive industry. The outlet is set to *pressure outlet*.

The radiator has been internally meshed with uniform hexahedral cells and in order to model the flow accurately the cell zone is set to *porous media* with flow parameters to model the resistance of the radiator.

The numerical scheme used in the study is the *second order upwind scheme* and the pressure velocity coupling scheme is the *SIMPLE*.

The vast majority of the simulations run in this study are steady simulations. However though some transient simulations have been run with sliding mesh to model wheel rotation. For these simulations the pressure velocity coupling was changed to *SIMPLEC* in accordance with the knowledge and practice used by Christoffer Landström at Chalmers.

The transient formulation is the *second order implicit* and the timestep in all transient simulations have been explicitly set to $0.08 ms$ in order to fulfill the *CFL-condition.* Basically the *CFL-condition* is that the solution should not be transported more than one cell in one single timestep.

3 Case description

The task of investigating the flow interaction between wheels, wings and diffuser is huge, thus delimitations of this study were a necessity.

First of all the base of the geometry is an actual vehicle and thus the improvements can only be accurately judged for this particular geometry. Furthermore the devices mounted in the rear are influenced of the flow upstream, which is governed by the geometry of the vehicle. Thereby one can only claim that the actual improvements are valid only for this particular geometry. However though one can assume that certain trends are valid for similar vehicles.

Since the study is to investigate effects originating from four parts, namely the two wings the diffuser and the rims/wheels, the study is initially divided into two separate parts. One part that focused on the wheels and one part that focused on the wing and diffuser.

Obviously all configurations were compared to the original geometry, which in the report is referred to as *Case001* or *Baseline*.

The different configurations are presented below and in detail in table i in Appendix A.

3.1 Wheel/Rim study

The original rims fitted to the vehicle were rims with small spokes and large open areas.

From the baseline simulation it was also clear that a significant airflow through the rims is present, creating large areas of low total pressure around the wheels where energy is lost. The most obvious and extreme modification to the rim that can be made in order to adress this problem is to cover the entire rim and block all cross flow. Previous studies has shown positive effects, mainly reduction in drag, when covering the rims [4].

Several configurations were carried out with covered rims, front and rear wheels separately covered as well as both covered.

The thesis is that covering the rims would result in a smoother flow as well as to prevent the flow underneath the vehicle from spilling out towards the sides and hence maintain a high flow velocity underneath the vehicle.

3.2 Wing/Diffuser study

It was found from the baseline study that the original diffuser, fitted on the vehicle, only operates as intended in a small part in the centre of the diffuser. To improve the functionality of the diffuser, it was fitted with longitudinal canards to channel the flow backwards and create separate regions in which a high flow velocity can be maintained.

The drag penalty is often quite small for the diffuser, compared to the downforce generated from it, and thus it is of great interest to have the diffuser operating at its best. Furthermore, the vehicle was fitted with a lower wing which in the initial study seemed to introduce a lot of drag but not adding much to the downforce. Hence a configuration with the lower wing removed was simulated in order to map out the negative and positive aspects of a wing mounted close to the vehicle body.

Finally the relatively agressive wing profile used for the upper wing was altered to a less agressive profile with a slightly more agressive angle of attack in order to prevent early separations which was found on the underside of the original wing.

3.3 Combinations

Finally, based on the finding from the initial simulations, a range of combined configurations were set up in order to optimize the positive effects of all configurations. A complete list of all cases included in this report can be found in Appendix A.

4 Results - Initial study

The results from the different simulations are presented below. In this chapter a number of coordinate planes are used to visualize the results. The definitions of the most frequently used planes can be found in Appendix B.

4.1 Rim design configurations

The simulations have been carried out with four different wheel setups listed in Table 1.

Table 1: *The different rim configurations*

Case001	Baseline
Case002	Front wheel covered
Case003	Rear wheel covered
Case004	Both front and rear wheel covered
Case005	*Case001* yawed at 5deg
Case006	*Case002* yawed at 5deg
Case007	*Case003* yawed at 5deg
Case008	*Case004* yawed at 5deg

The global aerodynamic performance of the four configurations are compared in Table 2 and in Figure 10 where the difference in lift and drag for the three modified cases and the baseline case are displayed.

Table 2: *Delta values for the three cases, compared with Case001.*

Case	ΔC_D	ΔC_L	$\Delta C_{L,f}$	$\Delta C_{L,r}$
Case001	-	-	-	-
Case002	-0,010	0,075	0,076	-0,001
Case003	0,000	-0,024	-0,005	-0,019
Case004	-0,018	0,048	0,073	-0,025

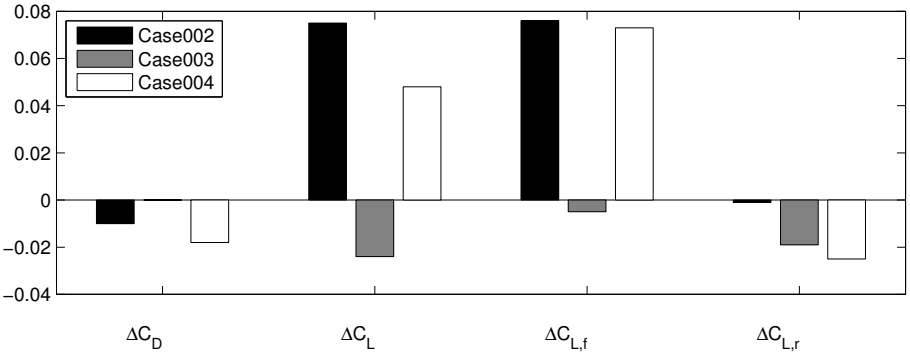

Figure 10: *A bar plot illustrating the differences in lift and drag force for the different configurations.*

Covering the front wheels results in a decrease in drag but a penalty of increased lift. It seems that all the increase in lift applies on the front axle. However, covering the rear wheels does not seem to affect the drag even though there is a significant increase in downforce, especially in the rear. Covering both front and rear wheels results in an even larger decrease in drag. The lift generated from the covered front wheel is the same as when only the front wheels are covered but some of the lift is now cancelled out from the decrease in lift at the rear.

4.1.1 *Case001* Baseline

This configuration consists of the geometry of *Lotus Evora Type 124 Endurance Racecar* equipped with production rims, see Figure 3. By analysing the results from this configuration other configurations of interest can be identified. In Figure 11 the iso-surfaces for total pressure equal to zero are showing areas of low total pressure and hence sources of energy losses.

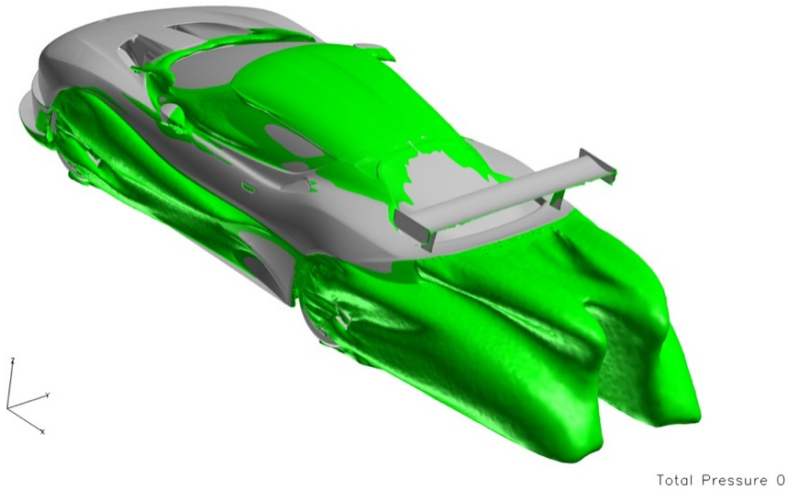

Figure 11: *Case001 Iso-surface for total pressure equal to zero*

Of course the biggest area is the base wake aft of the vehicle but there are also smaller wake structures induced from different parts of the vehicle. The wheels seem to, as expected, contribute to the energy losses judging from Figure 11. Especially the crossflow through the front rim opening seems to be creating large wake structures. Hence a number of different rim configurations are evaluated.

4.1.2 *Case002* Front wheel covered

In this configuration the spoked rims at the front have been replaced with completely sealed rims that can be seen in Figure 12.

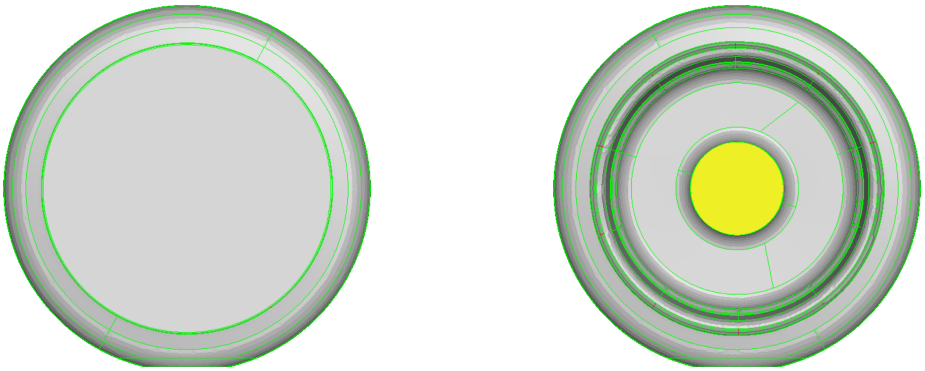

Figure 12: *Covered rim*

The distribution of coefficient of total pressure outside of the rim is displayed in a y-plane in Figure 13. The distribution of coefficient of total pressure is also displayed for *Case001* as a reference.

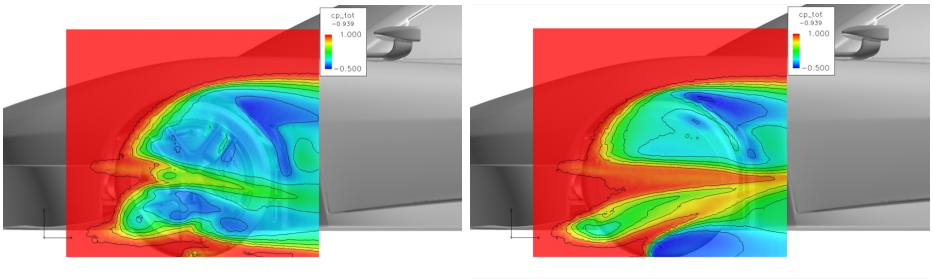

(a) *Case001* (b) *Case002*

Figure 13: $C_{p,tot}$*-distribution around the front wheel, y-plane*

A significant difference can be noted at the lower part of the wheel where the covered wheel creates a much larger region of low total pressure around the contact patch. At the middle part of the wheel a higher total pressure can be noted for *Case002*. In general the flow passing the rim is less disturbed, since the crossflow through the rim is eliminated.

Looking at forces there is a total decrease in drag for this configuration compared to the *Case001*. However, the aerodynamic force acting on the body are actually increased slightly compared with *Case001* but for the force in x-direction acting on the front wheel only 81% of the force for *Case001* are found for *Case002*. At the rear wheel an even larger percentual force reduction is achieved, considering force in x-direction on the rear wheel. Only 77% of the force in *Case001* is found for this configuration. This indicates that the rear wheel is highly dependent of the front wheel. The distribution of coefficient of total pressure around the rear wheel displayed in a y-plane can be found in Figure 14.

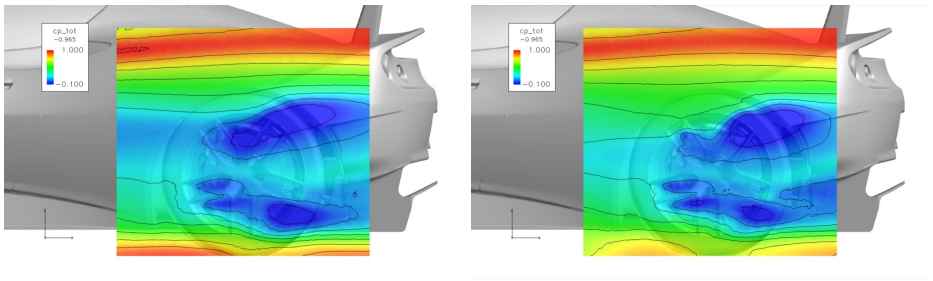

(a) *Case001* (b) *Case002*

Figure 14: $C_{p,tot}$*-distribution around the rear wheel, y-plane*

Some differences can be seen. Most obvious is the shape of the wake created from the upper part of the wheel as well as the overall lower total pressure close to the contact patch that indicates that the covered front wheel influences the flow around the rear wheel.

The most distinct difference when it comes to lift forces is found when comparing the lift generated from the wheel houses. A significant reduction in downforce from the wheel houses is achieved Only 80 % of the z-force for *Case001* is present in this case. This could be caused by the flow entering the front wheel houses from the front diffuser as well as through the cooling ducts. Since the front rims are covered the crossflow through the rims is eliminated and a higher pressure inside the wheel houses is achieved. The difference in pressure is clearly vissible in Figure 15.

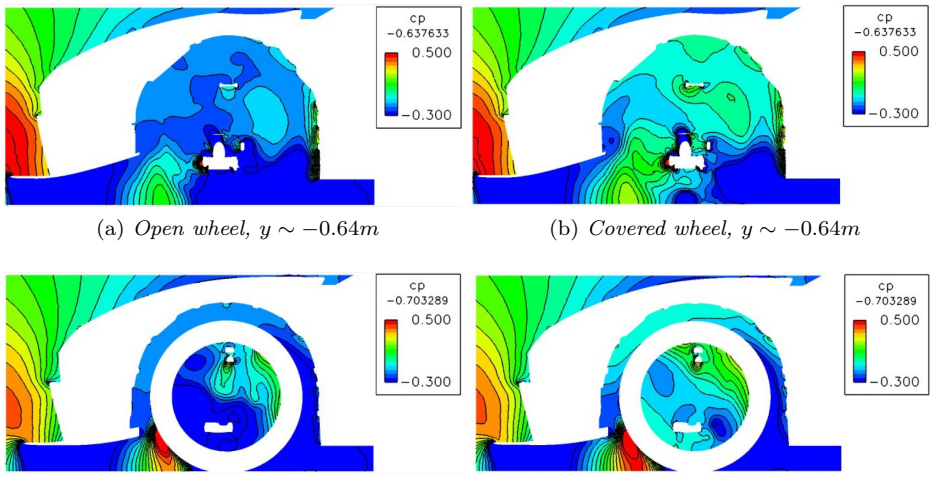

(a) *Open wheel,* $y \sim -0.64m$ (b) *Covered wheel,* $y \sim -0.64m$

(c) *Open wheel,* $y \sim -0.7m$ (d) *Covered wheel,* $y \sim -0.7m$

Figure 15: C_p*-distribution inside and around the front wheel, y-plane*

In Figure 15 the coefficient of static pressure inside the rim and wheel house is confirmed to be higher when the rim is covered. It is also clear that the high pressure propagates in front of the wheel close to the contact patch. This region with higher pressure in front of the wheel is probably pushing the air on the

outside of the rim causing the larger wake structure generated from around the contact patch, vissible in Figure 13.

4.1.3 *Case003* Rear wheel covered

In this configuration the rear wheel is covered in the same manner as the front wheel in the previous configuration, see Figure 12. Comparing the flow around the rear wheel with *Case001* a significant difference in the total pressure outside the rim is found. The coefficient of total pressure is shown in a y-plane in Figure 16.

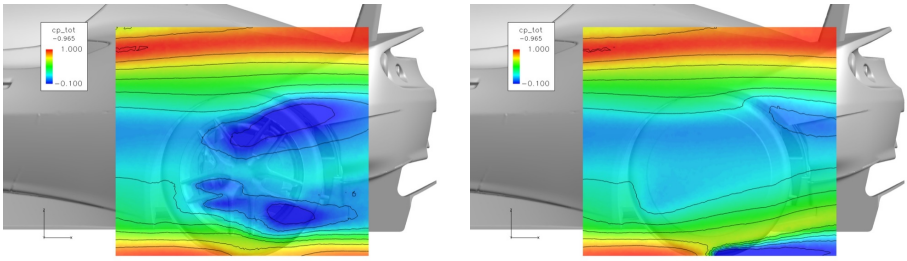

(a) *Case001* (b) *Case003*

Figure 16: $C_{p,tot}$*-distribution around the rear wheel, y-plane*

The lack of crossflow result in a distinct higher total pressure at the middle part of the rim. However, the same phenomena as for *Case002*, where the total pressure close to the ground, starting from the contact patch, is significantly lower than for *Case001*, is found for the rear wheel for *Case003* as well. Studying Table 2 it is obvious that there is an increase in downforce especially in the rear when covering the rear wheel. Looking at the forces acting on specific parts it can be noted that the downforce from the diffuser is increased by almost 6% from *Case001*. This is probably due to that when the rear wheels are covered the air underneath the vehicle is more enclosed by the closed rims and hence the flow through the diffuser is increased.

4.1.4 *Case004* Both front and rear wheel covered

In this case the previous two cases are combined and hence both front and rear wheels are covered. This configuration results in the highest decrease in drag. However, the increase in lift from the covered front wheel is more or less the same in this case as when only covering the front wheel though the covered rear wheel increase the downforce. The pressure distribution around the front and the rear wheel, for this case compared with *Case001* can be seen in the Figure 17.

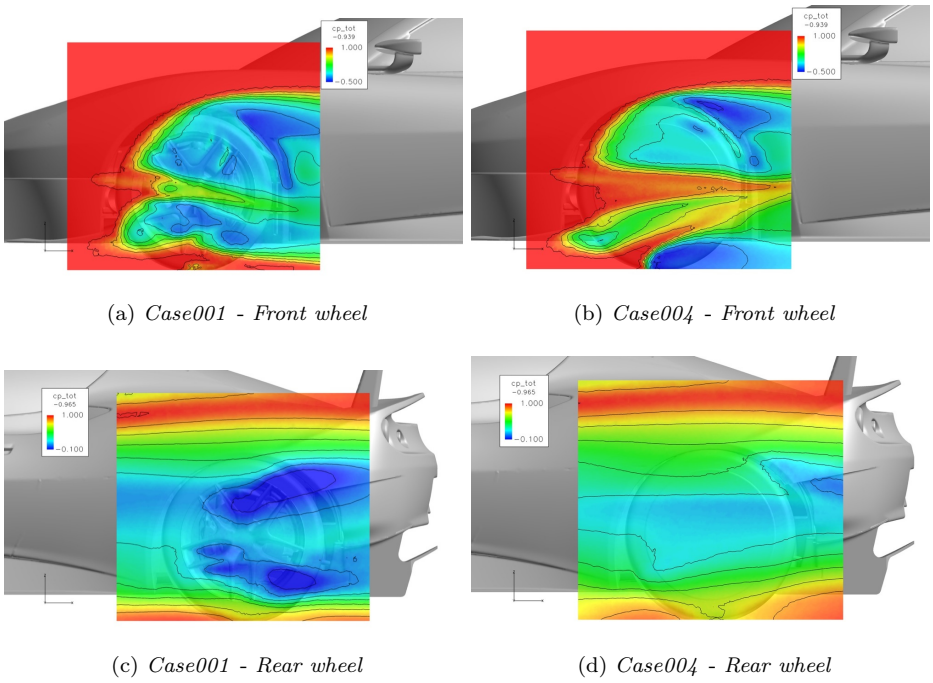

(a) *Case001 - Front wheel* (b) *Case004 - Front wheel*

(c) *Case001 - Rear wheel* (d) *Case004 - Rear wheel*

Figure 17: $C_{p,tot}$*-distribution around the front and rear wheel, y-plane*

The covered front wheel is the first modified part that the flow reaches. Hence the flow around covered front wheel behaves more or less the same wether or not the rear wheel is covered. Regarding the covered rear wheel it behaves different from *Case003*. This indicates that the flow from the front wheel has a large influence on the rear wheel. In Figure 18 the total pressure distribution around the rear wheel of the two cases where the rear wheel is covered, can be compared.

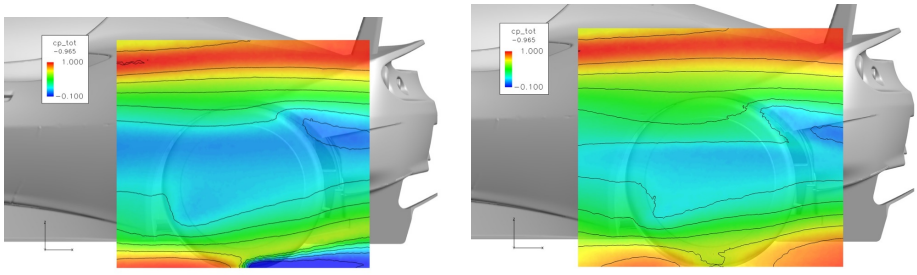

(a) *Case003* (b) *Case004*

Figure 18: $C_{p,tot}$*-distribution around the rear wheel, y-plane*

There can be noted a significant difference between the total pressure distributions for the two cases. A large reduction in drag, for the case where both wheels are covered, is probably achieved due to the reduction of the low total

pressure region around the contact patch of the rear wheel in *Case003*. This is confirmed when studying the forces acting on the rear wheel in the x-direction where *Case004* produces a drag at the rear wheels that is only 78% of the drag for *Case003*.

In order to explain the difference in wake structure around the rear wheel, between when the front wheel is covered or not, a Δvel-mag-plot is found in Figure 19.

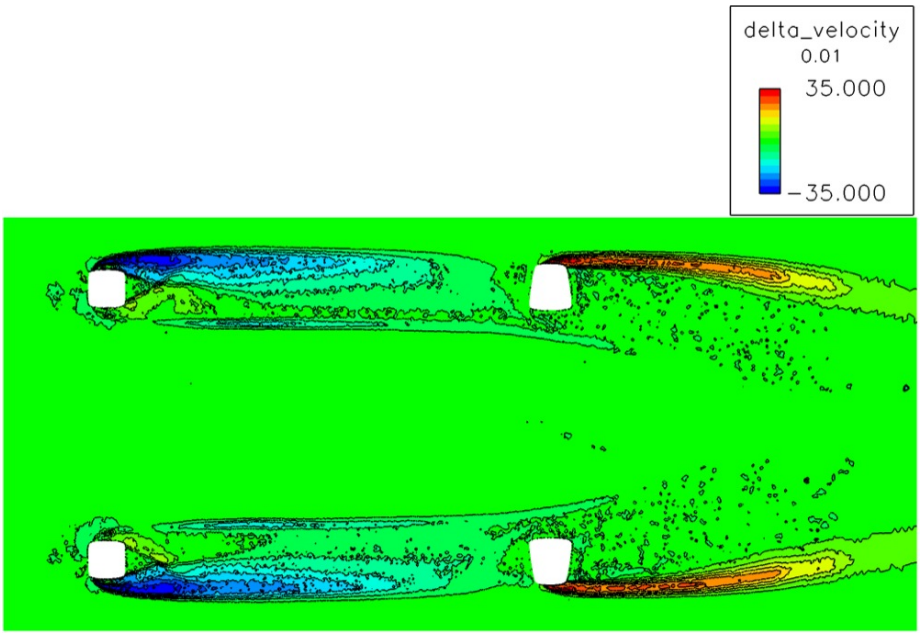

Figure 19: *Difference in velocity magnitude between Case004 and Case003 in a z-plane* 10*mm above ground.* $\Delta v = v_{Case004} - v_{Case003}$

The blue areas show areas where the velocity for *Case004* is lower than for *Case003* and hence red shows the opposite relation. The wake structure that is visible in Figure 18 for *Case003* generated from the rear wheel, is visible as the red area in this Figure. The wake structure that has been shown before to be induced from the front wheel when the wheel is covered is visible as the blue area in this Figure. It is obvious that the wake structure from the front wheel propagates all the way back to the rear wheel for *Case004*. This affects the stagnation pressure for the rear wheel as shown in Figure 20.

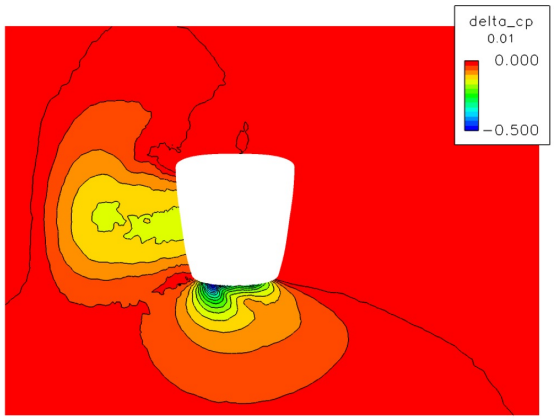

Figure 20: *Difference in C_p around the contact patch of the rear wheel in a y-plane at 10mm above ground.*$\Delta C_p = C_{p,Case004} - C_{p,Case003}$

This Figure clearly shows that the low pressure area in the front becomes higher for the rear wheel when the front wheel is not covered. Since the pressure behind the wheel is not affected, the difference in pressure, over the rear wheel becomes higher for *Case003*. This can force the separation point further forward and hence cause the wake structure only found in *Case003*.

4.1.5 Yaw-sensitivity for rim design configurations

The results for the four rim configurations above simulated in yaw condition are presented below.

To investigate the sensitivity to yaw for each configurations the C_D, C_L, $C_{L,f}$ and $C_{L,r}$ values are compared between the five degree yaw case and the corresponding zero degree yaw case. The delta values for each configuration are displayed in Table 3 and visualised in Figure 21.

Table 3: *Delta values for the four different configurations in five degrees yaw compared with the corresponding case in zero degrees yaw.*

Case	ΔC_D	ΔC_L	$\Delta C_{L,f}$	$\Delta C_{L,r}$
Case001	-	-	-	-
Case005	0,004	0,083	0,013	0,071
Case002	-	-	-	-
Case006	0,009	0,070	0,015	0,054
Case003	-	-	-	-
Case007	0,006	0,105	0,020	0,085
Case004	-	-	-	-
Case008	0,020	0,102	0,024	0,078

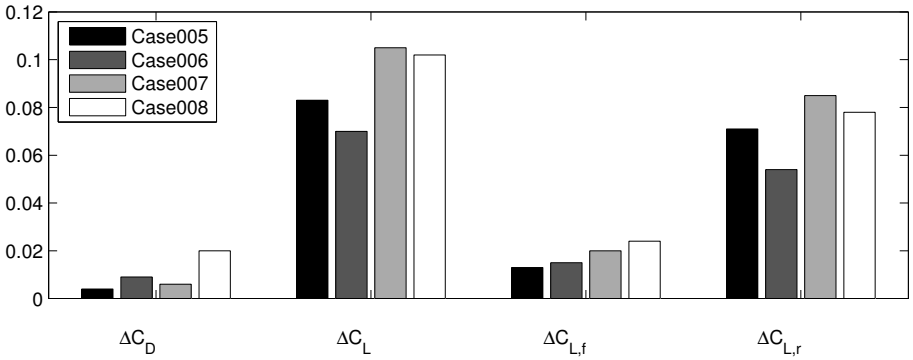

Figure 21: *A barplot of the delta values of lift and drag for the different yaw-configurations in this section.*

In terms of drag most of the configurations are not affected that much by the five degree yaw angle. However, the configuration where both wheels are covered, *Case008,* shows a significant increase in drag. The flow structures underneath the vehicle can be studied in Figure 22.

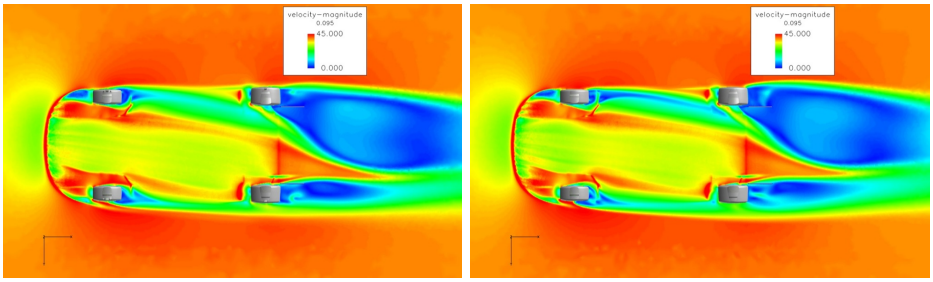

(a) *Case005* (b) *Case008*

Figure 22: *Velocity magnitude under the vehicle, z-plane*

A difference can be noted in the wake structure created from the front wheel. It seems that if the front wheel is covered the wake induced from it is creating more drag compared to when front rim is not covered. This wake structure, that is extended substantially longer compared to the wake structure induced by the production rim, is found in both cases where the front wheel is covered. However, the configuration where both wheels are covered is very beneficial in zero degree yaw and reduced the drag significantly compared with the baseline. Hence the delta value for the yawed configurations becomes larger than for the other cases. Still that configuration is proven to be the most sensitive to yaw in terms of drag.

The lift values show clearly that the configurations with covered rear wheel is most sensitive to yaw in terms of lift. In yaw condition the flow underneath the vehicle is significantly disturbed, see Figure 23. Since the diffusers, front and rear, are some of the most important devices to create downforce the lift is clearly affected by the yaw condition.

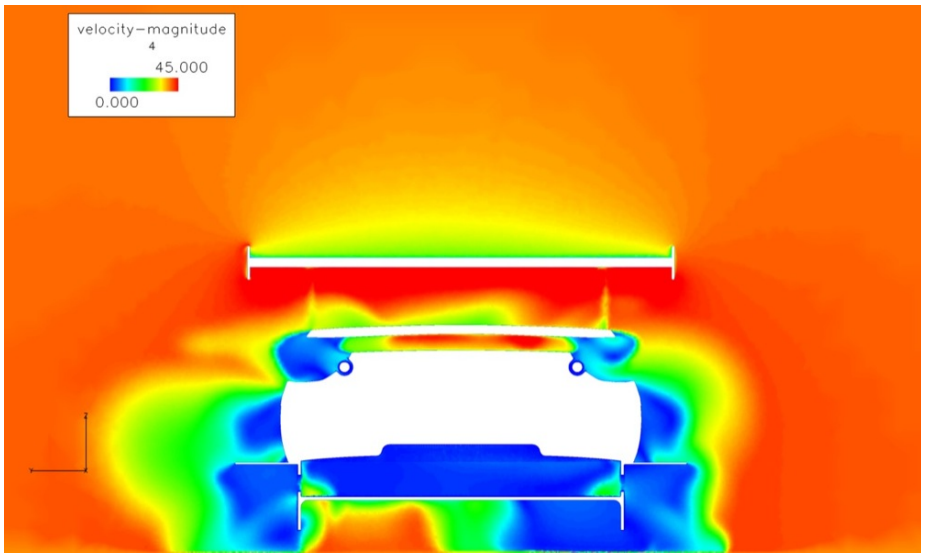

Figure 23: *Case005, velocity magnitude in a x-plane at $x = 4m$ the rear of the vehicle.*

4.1.6 Observed trends

Below the observed trends in the rim design configurations is summerised. A large increase in lift can be noted when comparing *Case001* with the two cases, *Case002* and *Case004,* where the front wheels are covered. This is found to, a large extent, be generated from the increase in pressure on the front wheel houses. This can be visualised clearly when plotting the coefficient of static pressure over the surface of the front wheel house, see Figure 24.

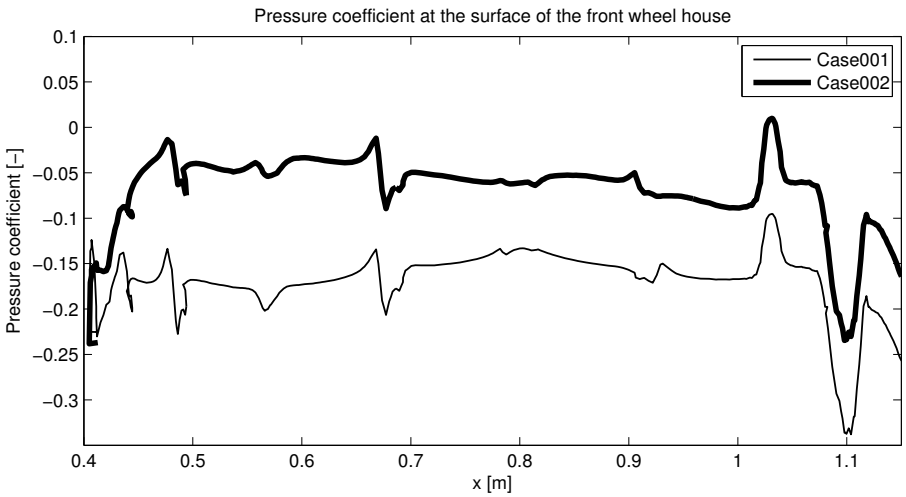

Figure 24: *C_p at the surface of the front wheel house*

Only two of the cases are included in this plot due to the correlation within

the pair of cases where the front wheel is covered and not covered. Hence *Case003* followed the plot for *Case001* and *Case004* followed the plot for *Case002.*

By plotting the $C_{p,tot}$-distribution on a z-plane 100 mm above ground around the front wheel, for *Case001* and *Case002,* a higher pressure inside the rim could be noted, see Figure 25. Only one case where the front rim is covered and one where it is not covered are presented since the flow around the front wheel seems to be independent to whether or not the rear rim is covered. Note that another scale is used for Figure 25 to resolve the $C_{p,tot}$-distribution more accurately. Areas of interest are highlighted.

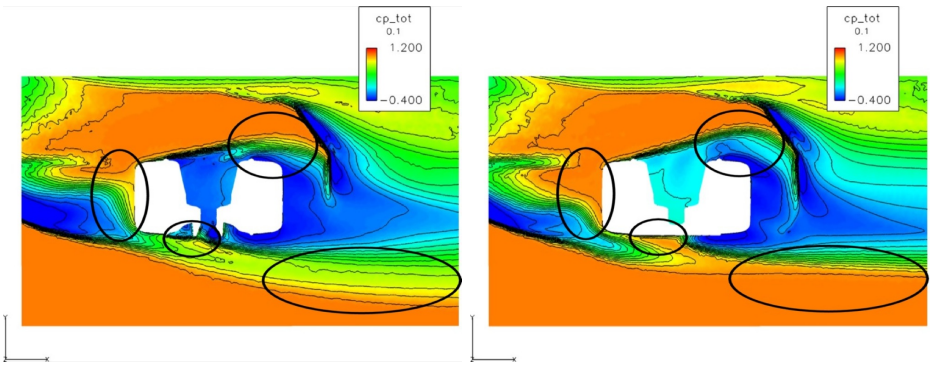

(a) *Case001* (b) *Case002*

Figure 25: $C_{p,tot}$*-distribution around the front wheel, z-plane*

The largest difference between front production rim and the covered wheel is the shape of the wake induced by the front wheel. The production rim creates a much wider wake structure than the covered rim. Where the wake structure created for the different configurations is clearly visible in the Figure above. There is a significant difference in flow pattern where the open area between the spokes are positioned for *Case001.* The crossflow through the rim seem to be creating the wake structure further forward for *Case001* than for *Case002.* On the inside of the wheel the wake structure is slightly wider for the closed rim than for the production rim. This might also be an effect from blocking the crossflow as the flow from inside of the wheel house needs to pass between the wheel and the wheel arc. In the front of the wheel there is a large difference between the two cases where the air seem to flow almost only outside of the wheel in *Case002* whereas for the production rim some of the air seem to go on the inside of the wheel. In Figure 26 the C_p-distribution is displayed in the same coordinate plane that were used in the previous Figure.

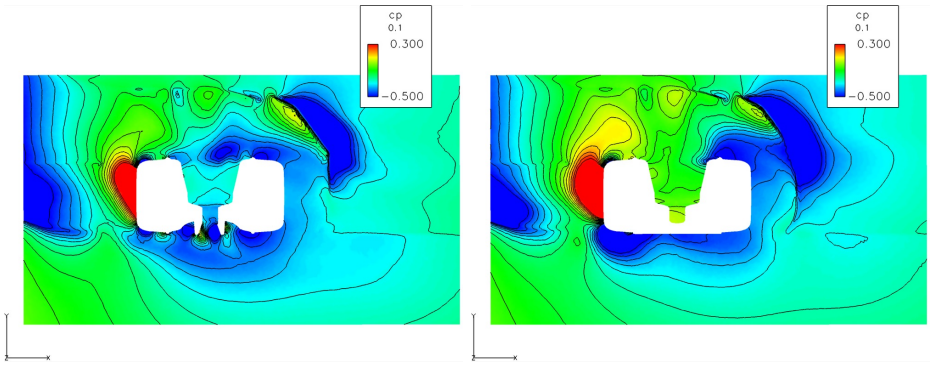

(a) *Case001* (b) *Case002*

Figure 26: C_p*-distribution around the front wheel, z-plane*

The higher pressure found inside the rim indicates as Figure 24 that the air gets trapped inside of the rim and the wheel house and hence the pressure is increasing, resulting in reduced down force at the front axle. The phenomena found in Figure 25, that the air goes outside of the wheel for the closed rim configuration, could also be caused by the pressure increase in the wheel house. The pressure peak around each spoke is also clearly visible in this Figure.

The $C_{p,tot}$-distribution around the rear wheel in plane corresponding to the one in Figure 25, is shown in Figure 27 and 28. Areas of interest are highlighted.

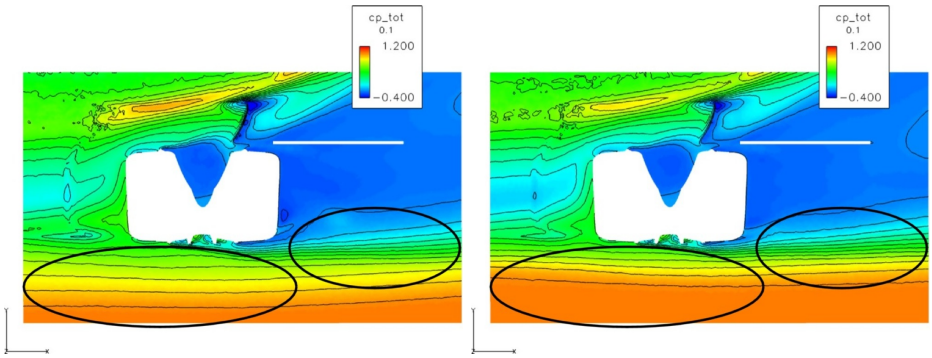

(a) *Case001* (b) *Case002*

Figure 27: $C_{p,tot}$*-distribution around the rear wheel, z-plane*

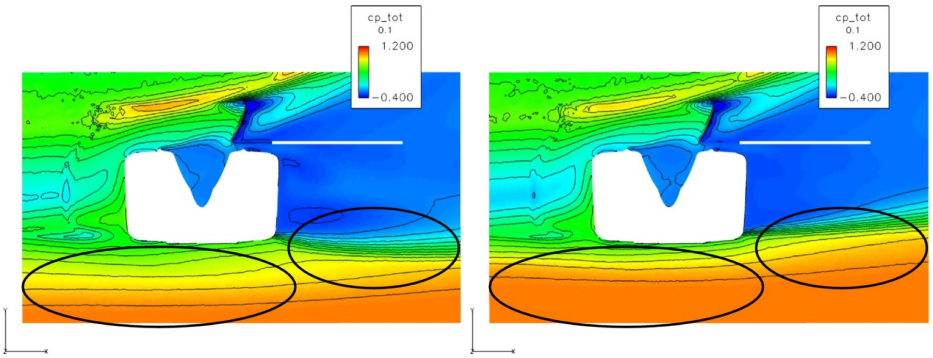

(a) *Case003* (b) *Case004*

Figure 28: $C_{p,tot}$*-distribution around the rear wheel, z-plane*

As stated before, the flow pattern around the rear wheel is highly dependent on the wake structure induced by the front wheel. The wake from the front wheel can from this Figure be confirmed to be more narrow when the front wheel is covered, judging from the contour lines parallel to the wheel. This seems to influence the structure of the wake created by the rear wheel when looking at *Case004*. The wake structure behind the rear wheel for *Case004* seems to go inwards whereas for *Case003* the rear wheel wake is heading straight or slightly outwards due to the wake structure only found for this case.

4.2 Wing and diffuser configurations

In order to acquire an understanding of the interaction between wing and diffuser a set of configurations have been simulated. They are presented in Table 4 below.

Table 4: *The different wing/diffuser combinations.*

Case001	Baseline with standard diffuser and wing
Case005	*Case001* yawed at 5*deg*
Case013	Improved diffuser with longitudinal canards
Case014	*Case013* yawed at 5*deg*
Case015	Removed lower wing, standard diffuser
Case017	Upper wing replaced with less aggressive wing profile

The overall delta-values of drag and lift can be seen in Table 5 below.

Table 5: *The overall drag and lift values for the different configurations*

	ΔC_D	ΔC_L	$\Delta C_{L,f}$	$\Delta C_{L,r}$
Case001	-	-	-	-
Case013	0.011	-0.058	0.002	-0.061
Case015	-0.030	0.109	0.000	0.109

The values from the Table above are also visualised in Figure 29 below. The general trend is that a slight increase in drag is followed by a slight decrease in downforce and the other way around.

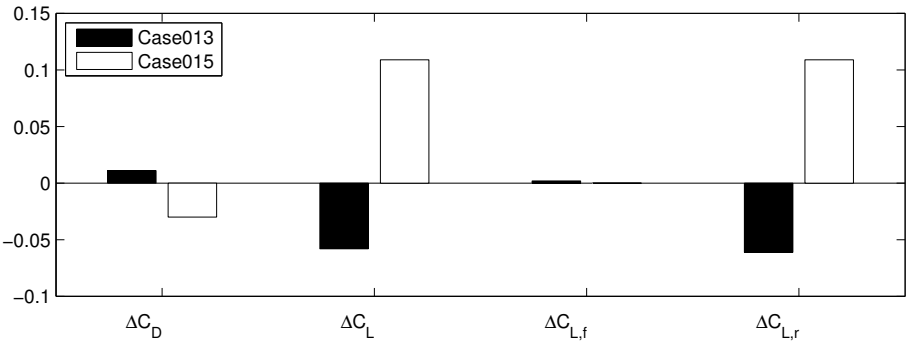

Figure 29: *A bar plot of the differences in drag and lift forces for the two different configurations in this section.*

It can be concluded that there are large differences in drag and lift for the different configurations but also that the differences related to lift is mainly in the rear and this is of course where the changes have been made.

The different configurations and their influence on the flow are presented in detail below.

4.2.1 *Case013* - Improved diffuser

The diffuser has been improved by the addition of longitudinal canards, the main purpose of course being to maintain a high flow velocity and prevent the rear wheel wakes to extend towards the center of the vehicle.

The original diffuser is depicted in Figure 30 above and the modified diffuser can be seen in Figure 31 below.

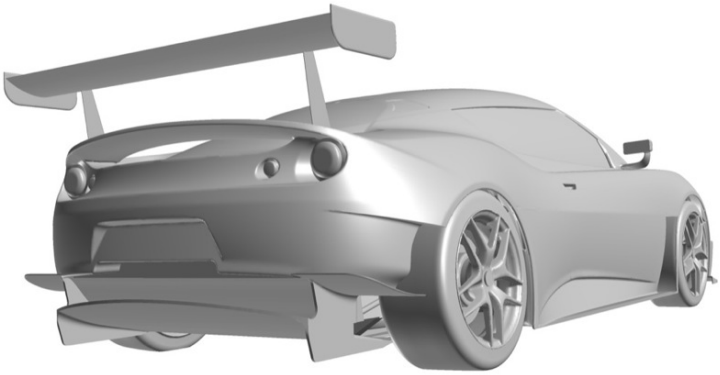

Figure 30: *The standard diffuser*

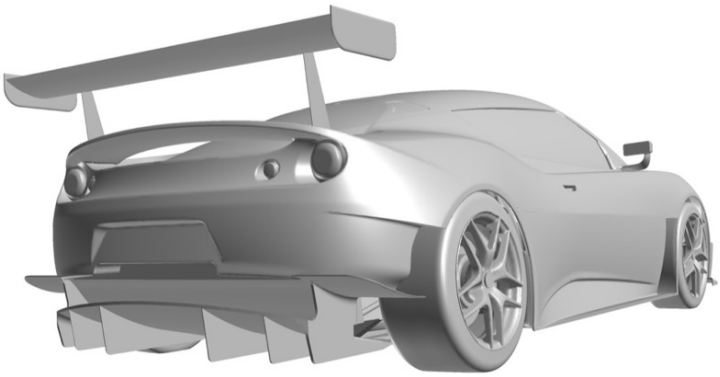

Figure 31: *The improved diffuser with longitudinal canards*

It is fairly clear from the results that the new diffuser generates more down-

force for 0° yaw, see Table 5 above.

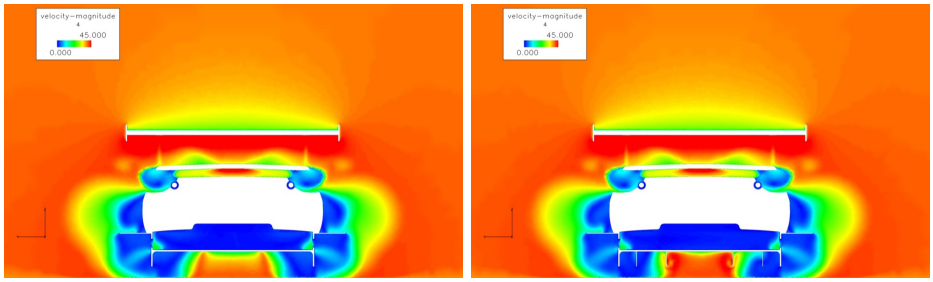

(a) *Standard diffuser* (b) *Improved diffuser*

Figure 32: *A comparison of the velocity magnitude for the two diffusers at the early stages of the base wake at x-coordinate 4.0*

It is clearly visible that the centre channel encapsulates the flow and thus maintains a higher flow rate in this area when compared to the original diffuser. This is one of the major reasons for the added downforce. When looking in detail on the static pressure on the diffuser in the y-plane at the centre of the vehicle in Figure 33 there is substantial lower pressure compared to the other two configurations. This is obviously due to the higher flow velocity.

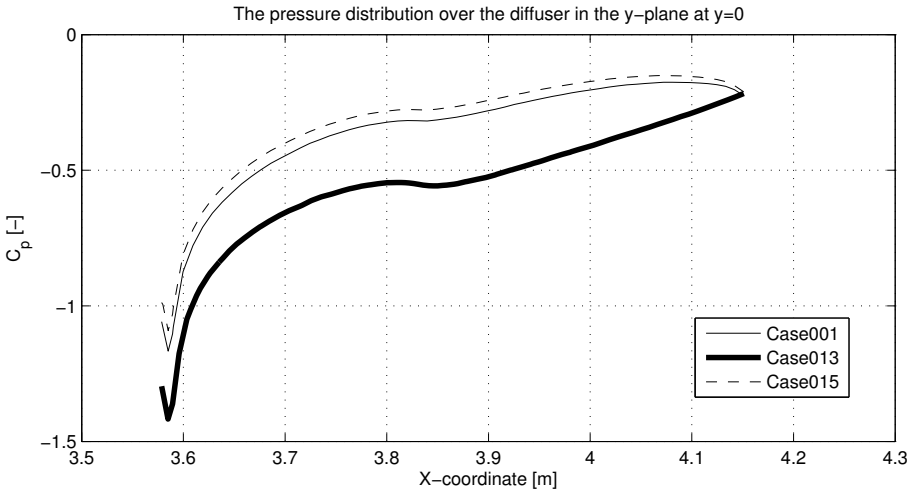

Figure 33: *The C_p-distribution over the diffuser at y=0*

This difference is even more evident when looking at the static pressure distribution in the x-plane. Especially in the centre part of the diffuser the pressure is substantially lower for the improved diffuser.

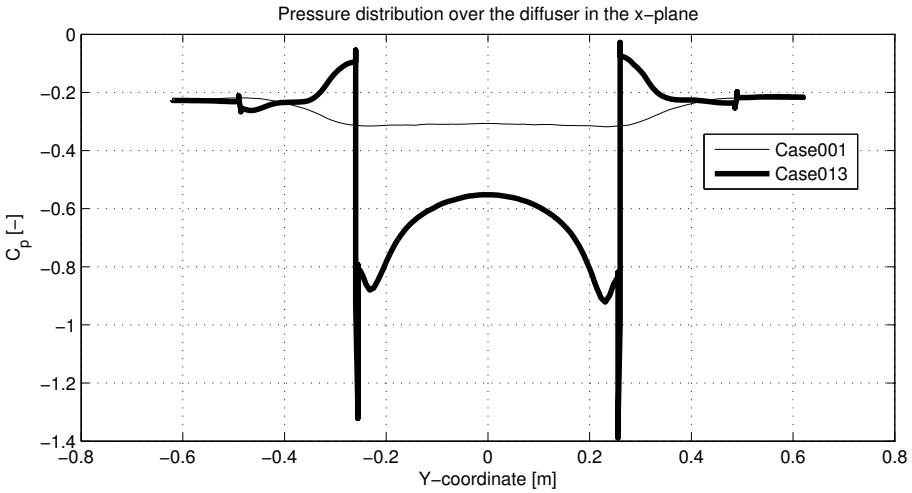

Figure 34: *The pressure distribution on the diffuser in the x-plane*

The position of the plane in which the pressure has been probed can be seen in Figure 35 below. The x-coordinate is $3.864m$.

Obviously the longitudinal canards are functioning well in maintaining the flow in the channels and thereby increasing the speed and decreasing the pressure. However though, it is believed that the position of the canards could be tuned in order to achieve even better performance under these particular circumstances.

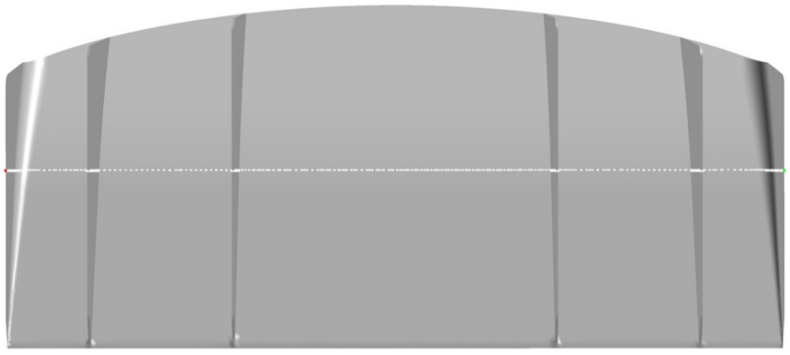

Figure 35: *The position where the pressure was probed in the x-plane*

The increased flow rate has a clear influence on the basewake at the centre of the vehicle. Which can be seen below.

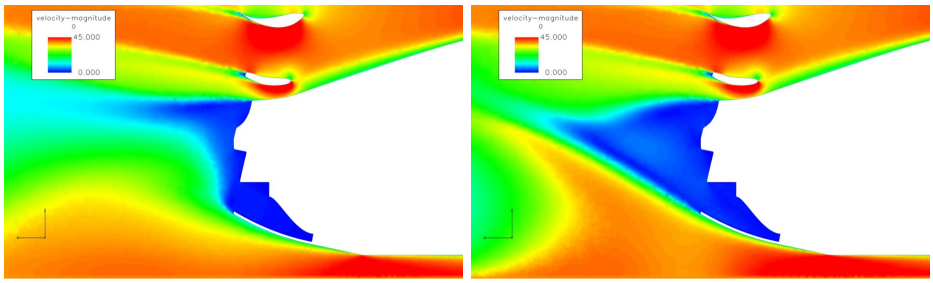

(a) *Case001 - Standard diffuser* (b) *Case015 - Improved diffuser*

Figure 36: *The velocity magnitude at the centre of the vehicle*

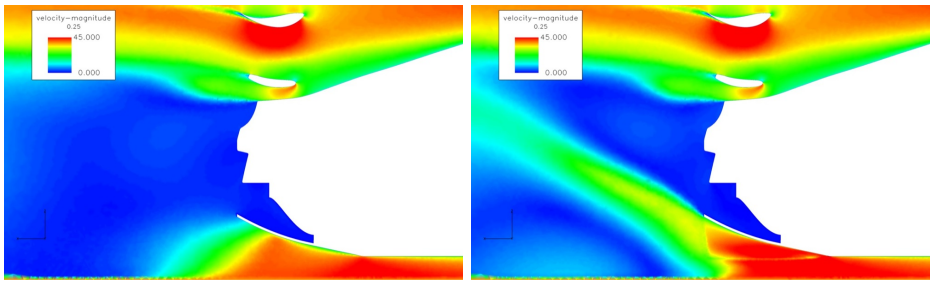

(a) *Case001 - Standard diffuser* (b) *Case015 - Improved diffuser*

Figure 37: *The velocity magnitude at 0.25m from the centre of the vehicle*

The improved diffuser introduce many positive effects, it channels the flow which enables it to generate more downforce with only a minor drag penalty. The canards introduce recovery zones where the high flow velocity is recovered or maintained.

4.2.2 *Case015* - Removed lower wing

Removing the lower wing from the baseline has substantial influence on a large part of the flow in the rear. When comparing forces between the baseline and the case with removed lower wing the following differences are especially interesting.

Table 6: *Percentual difference in forces acting on specific parts in the x-direction*

	Case001 [% N]	*Case015* [% N]
Body	-	−3.9
Windows	-	26.7
Upper wing	-	−89.0
Diffuser	-	−14.0
Rear wheel	-	−15.9

Table 7: *Percentual difference in forces acting on specific parts in the z-direction*

	Case001 [% N]	*Case015* [% N]
Body	-	4.9
Windows	-	13.9
Canard, rear bumper	-	27.0
Upper wing	-	−18.7
Diffuser	-	13.7
Underbody	-	3.1
Wheel houses	-	4.7

First of all it is evident that the body produce more lift when the lower wing is removed.

One of the most interesting differences is however the fact that the upper wing is functioning substantially better with the lower wing removed. The drag of the wing has been substantially reduced whereas the lift has decreased or rather downforce increased.

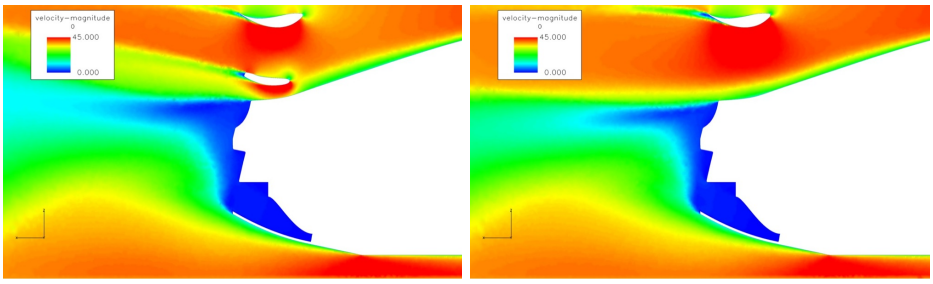

(a) *Baseline* (b) *Removed lower wing*

Figure 38: *The velocity magnitude at the center of the vehicle in the y-plane*

It is clearly visible in Figure 38 that the base wake is substantially reduced when the lower wing is removed. The most profound difference being the lack of upflow which was previously added by the lower wing. This reduce the area of low static pressure behind the vehicle.

Looking at the static pressure distribution around the vehicle it is clearly visible in the delta plot in Figure 39 that for the baseline case there is a significantly higher pressure in the vicinity of the upper wing and up towards the rear window, which partly explains the lesser drag and more downforce of the windows on the baseline. These effects can also be seen in the actual static pressure fields in Figure 40.

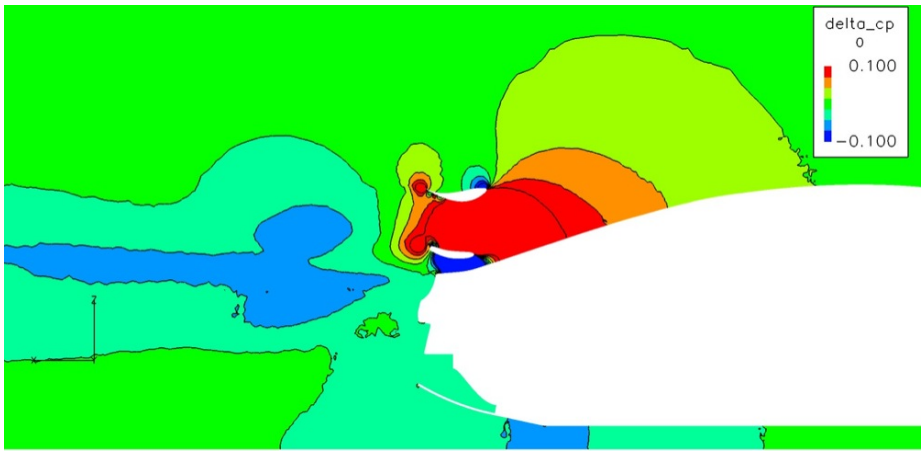

Figure 39: *A delta plot of the coefficient of static pressure.* $\Delta C_p = C_{p,Case001} - C_{p,Case015}$

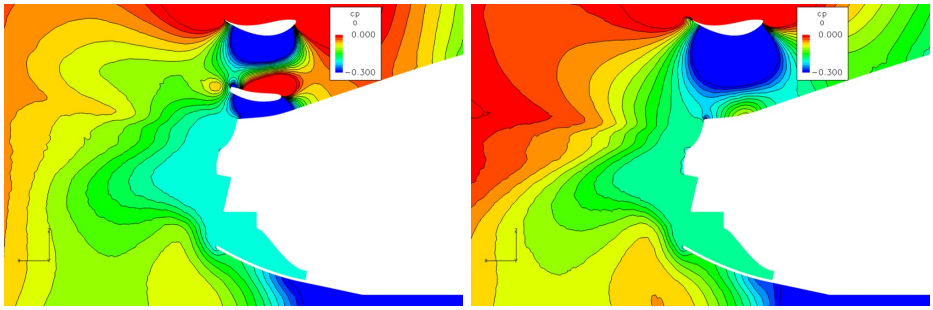

(a) *Case001* (b) *Case015*

Figure 40: *A comparison between the pressure fields for the baseline case and the case with removed lower wing.*

Furthermore, it is clearly visible in Figures 39 and 40 that the lower wing maintains a larger area of low static pressure behind the lower wing. This low pressure area also propagates down towards the diffuser making it generate more downforce, through increased flow velocity, as well as also more drag for the baseline when compared to *Case015*.

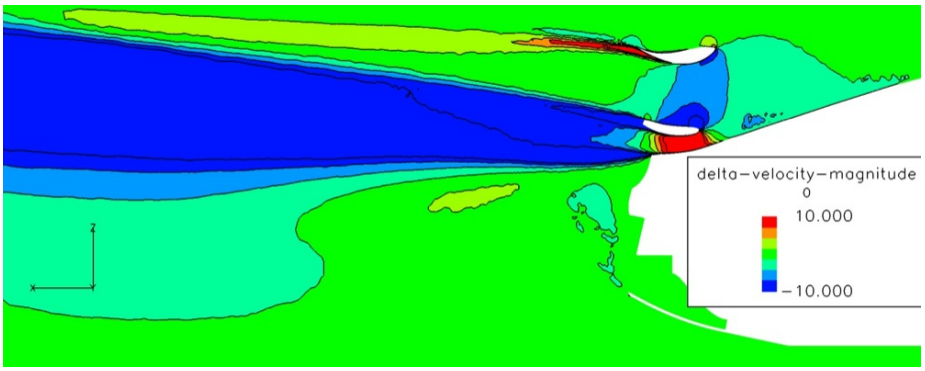

Figure 41: *A delta plot of the velocity magnitude.* $\Delta v = v_{Case001} - v_{Case015}$

Continuing with the velocity distribution behind the vehicle, it is clearly visible in Figure 41 that the lower wing creates and maintains a large area of relatively low velocity magnitude when compared to the case without lower wing. This is obviously not beneficial.

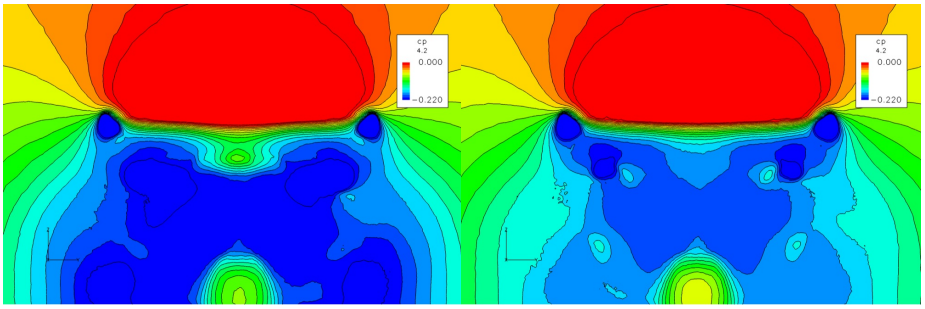

(a) *Baseline* (b) *Removed lower wing*

Figure 42: *The beginning stages of the base wake for both configurations.*

Looking at the the base wake just behind the wing in the x-plane it is clear that there is significantly higher static pressure in the wake for *Case015*. The higher pressure has reduced the drag of the vehicle somewhat but also reduced the driving force of the diffuser leaving it less efficient, this can be seen in Figure 33 on page 36 which clearly explain the difference in lift for the diffuser.

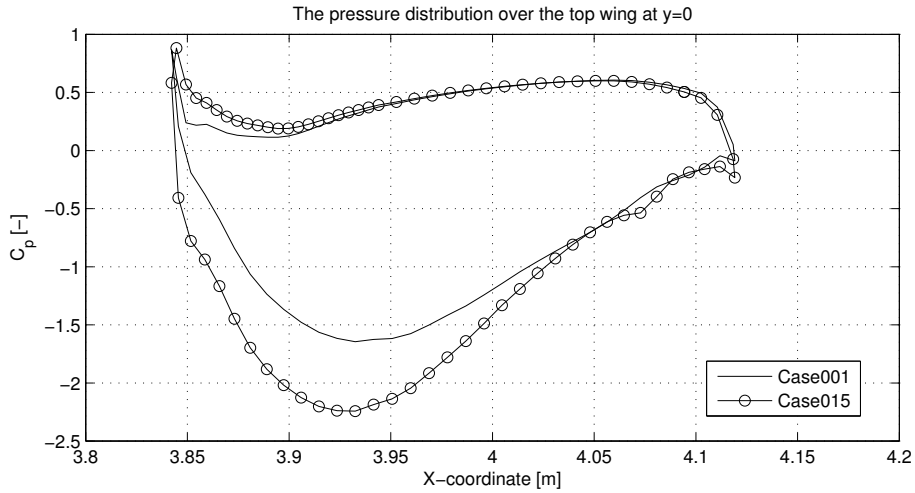

Figure 43: *A 2D-plot of the C_p-distribution over the upper wing for both configurations.*

The lack of a lower wing is, as previously mentioned, influencing the pressure below the upper wing, a comparison of the C_p-distribution around the upper wing for the two configurations can be seen in Figure 43 above. Not much have changed on the upper part of the wing but there is a major difference on the lower part where the pressure is significantly lower, explaining the increase in downforce. This is achieved since the flow is less disturbed underneath the upper wing when the lower wing is removed and thereby the velocity is increased.

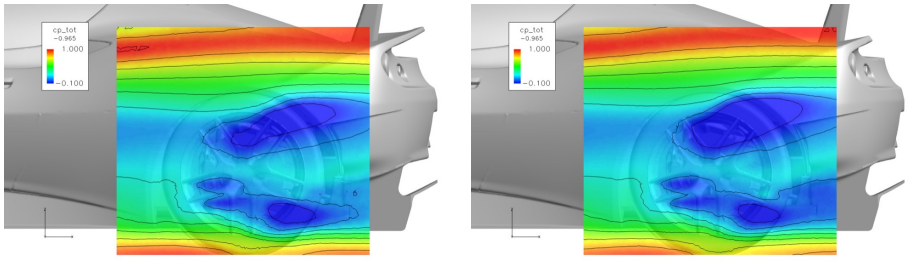

(a) *Case001* (b) *Case015*

Figure 44: *The $C_{p,tot}$-distribution in a plane approximately 30mm from the rear wheel*

Only minor differences can be seen in the pressure field around the rear wheel, found in Figure 44, but it is clearly visible that there is a larger area of low total pressure outside the wheel on the configuration without lower wing, which can be explained by the higher pressure in the base wake which is not adding as much energy to the flow, pulling it to the rear, as in the baseline.

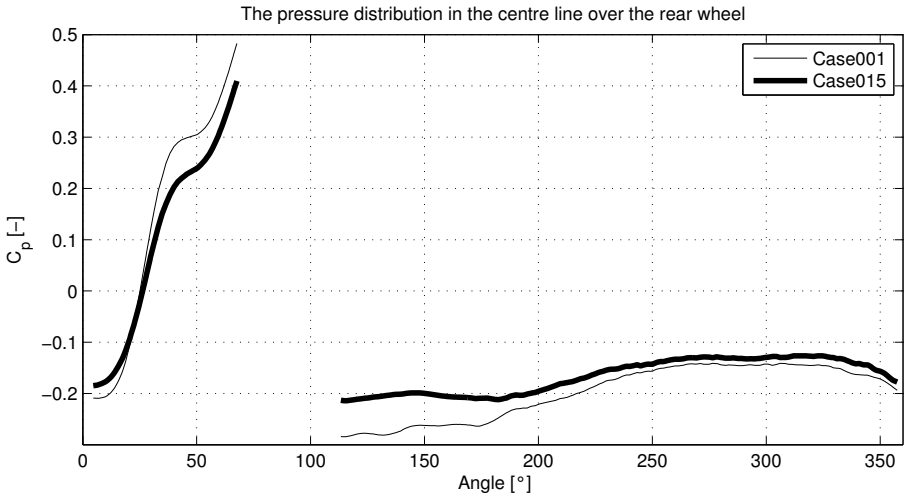

Figure 45: *The C_p-distribution on the rear wheel for the two configurations.*

The drag reduction on the rear wheel can also be explained by the difference in pressure shown in the graph above which shows the pressure around the centre of the wheel which is, for the most part, higher for *Case015*. The coordinate system used is illustrated in Figure 46.

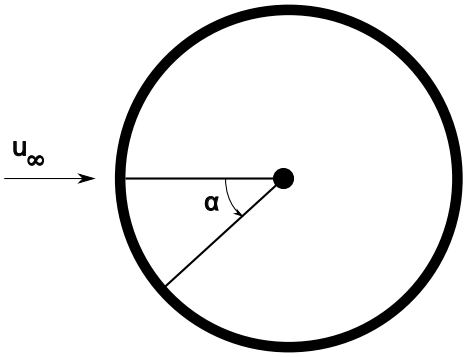

Figure 46: *The polar coordinate system used for the wheels in plots*

4.2.3 *Case017* Upper wing replaced with less agressive wing profile

In this configuration the suggested wing setup has been replaced with a less agressive wing profile. The original wing setup has an angle of attack at almost zero degrees, whereas the new profile is fitted with an angle of attack at 3 degrees. The less aggressive wing profile has previously been used on GT-cars produced by *Lotus Sports* and it is thus of great interest to evaluate this profile together with this vehicle this as well. The different wing configurations can be seen in Figure 47.

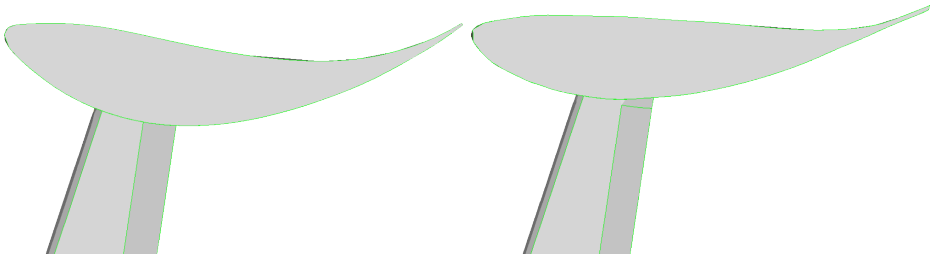

(a) *Original wing configuration* (b) *Less agressive profile*

Figure 47: *Wing configurations*

The overall influences from this modificaftion are presented as delta values compared with *Case001* in Table 8.

Table 8: Delta values compared with *Case001*

Case	ΔC_D	ΔC_L	$\Delta C_{L,f}$	$\Delta C_{L,r}$
Case001	-	-	-	-
Case017	-0,003	-0,032	0,006	-0,039

There is a significant increase in downforce from the new wing profile when compared with the original profile. Naturally the increase is only at the rear axle since the wing is positioned behind it. However, the difference in drag force can be considered to be within the error margin.

Looking at the distribution of static pressure around the wings it can be noted that there is a faster reduction in pressure for the less aggressive profile whereas the original wing has a larger area of relatively higher pressure in the rear parts of the upper part of the wing, see Figure *48.*

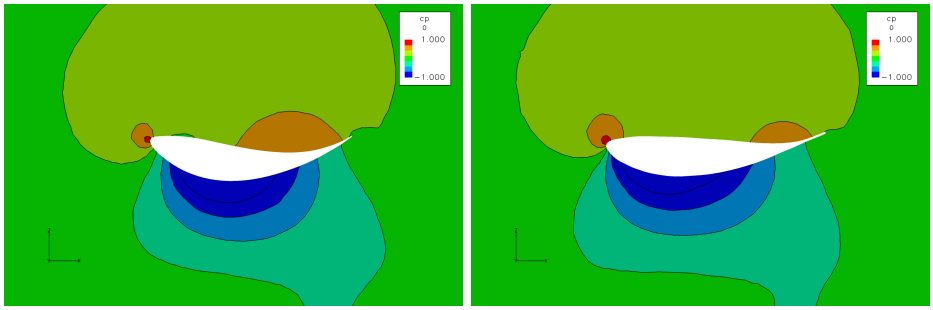

(a) *Case001* (b) *Case017*

Figure 48: *The coefficient of static pressure ploted around the wing, y-plane*

It is visible above that the stagnation point is slightly further up which results in an increase in downforce and reduction in drag.

The faster decrease in pressure for *Case017* which is also visible in Figure 49 is probably the reason for the increase in downforce. However though, the

irregular pressure distribution for *Case017* could be an indication of a problem, either with the solver or the design of the profile. The original profile has a better distribution with a more evenly distributed difference in pressure. Still however, the less agressive profile does perform better under these circumstances.

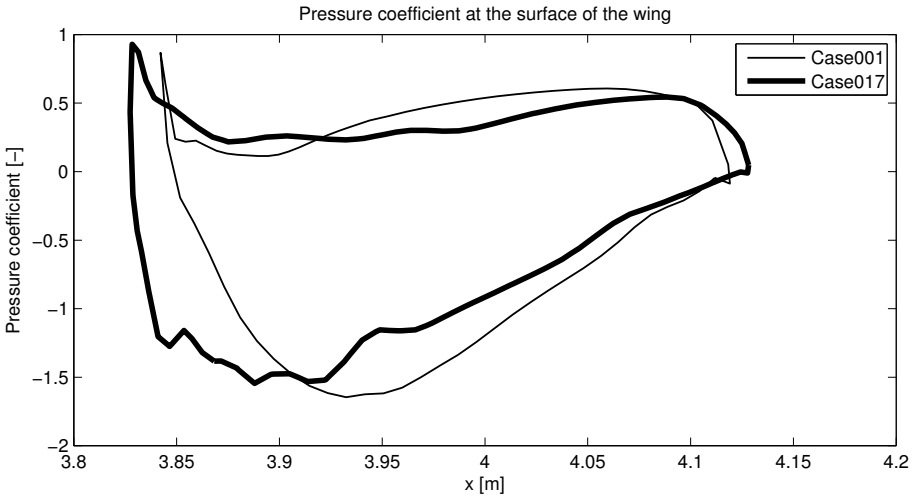

Figure 49: *C_p-distribution at the surface of the wing*

The plot shows clearly that there is a significant difference in pressure distribution between the cases. The wing profile in *Case017* is slightly longer than the baseline wing. However, the pressure drop is steeper for the new wing than for the original wing profile. In the rear of the wing the static pressure is actually lower underneath the baseline wing than underneath the new profile. Summing up the pressure difference over the wing the less agressive profile generates more downforce than the baseline wing.

4.2.4 Yaw-sensitivity for wing-diffuser configurations

The main goal of the improved diffuser is to maintain a high flow rate throughout the diffuser and to reduce the sensitivity to yawed conditions, where the longitudinal canards are to direct the flow in the general longitudinal direction of the vehicle.

Several simulations have been made for yawed conditions and they are, as previously has been mentioned, at 5° yaw.

Table 9: *Delta values of drag and lift for the baseline and the improved diffuser, they are compared with their respective non-yawed case*

	ΔC_D	ΔC_L	$\Delta C_{L,f}$	$\Delta C_{L,r}$
Case001	-	-	-	-
Case005	0.004	0.083	0.013	0.071
Case013	-	-	-	-
Case014	−0.007	0.110	0.006	0.105

The delta values of the lift and drag forces for the configurations are found in the Table above as well as in the bar plot below. The configurations are compared with their respective 0° yaw simulation. Thus the difference indicate the sesitivity towards yaw.

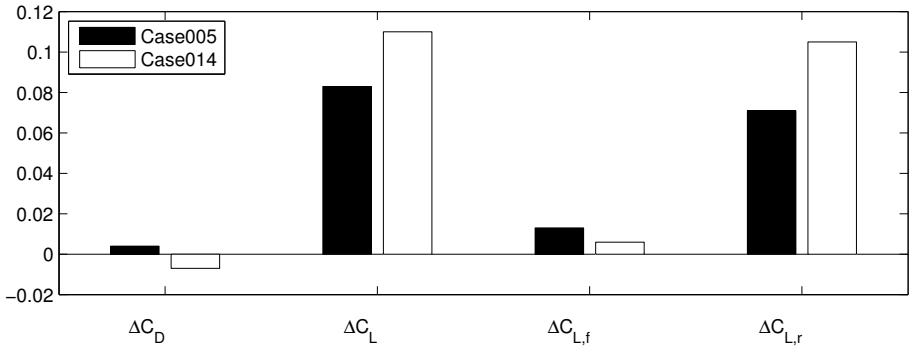

Figure 50: *A bar plot of the differences in force for the two configurations of interest in this section.*

The delta values are clearly visualised in the Figure above. It becomes obvious that for both cases the downforce in the rear is most affected. The downforce generating devices e.g. wing and diffuser are clearly losing efficiency in yaw condition. It can also be noted that the delta lift values in the rear, for *Case005* are lower than for *Case013.* This is further explained below.

When analysing the flow $5mm$ beneath the underbody, see Figure 51, it is evident that the longitudinal canards have a clear effect on the flow even though they are situated $5mm$ above the current plane.

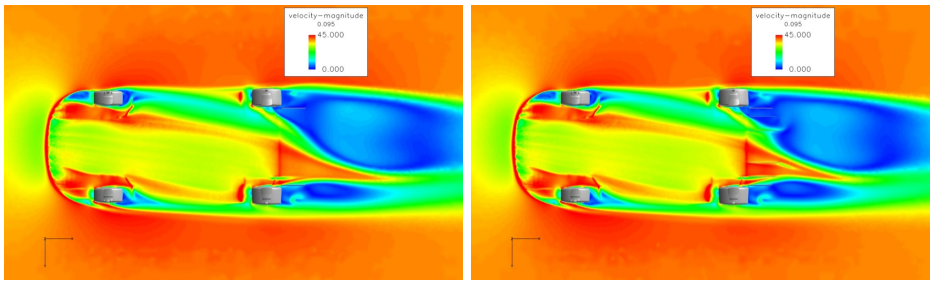

(a) *Baseline* (b) *Improved diffuser*

Figure 51: *A comparison of the velocity magnitude just beneath the underbody*

Even though the wake structures are similar it is clearly visible that there is higher velocity in the vicinity of the canards and that the flow is directed backwards in the general direction of the vehicle. This is also clearly visible in the x-plane in the beginning stages of the base wake in Figure 52.

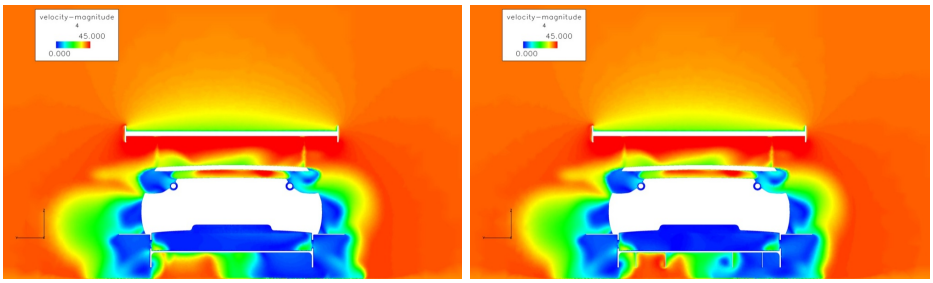

(a) *Case005 - Baseline* (b) *Case014 - Improved diffuser*

Figure 52: *A comparison of the velocity magnitude in the beginning stages of the base wake.*

The velocity recovery zones are even more evident in the plot in Figure 53, where the pressure is significantly lowered at the inside of each canard and thus the flow velocity increased. When compared to the baseline diffuser it is evident that instead of a continously decreasing pressure in the positive y-direction there are zones along the diffuser in which high velocity is maintained and thus pressure reduced.

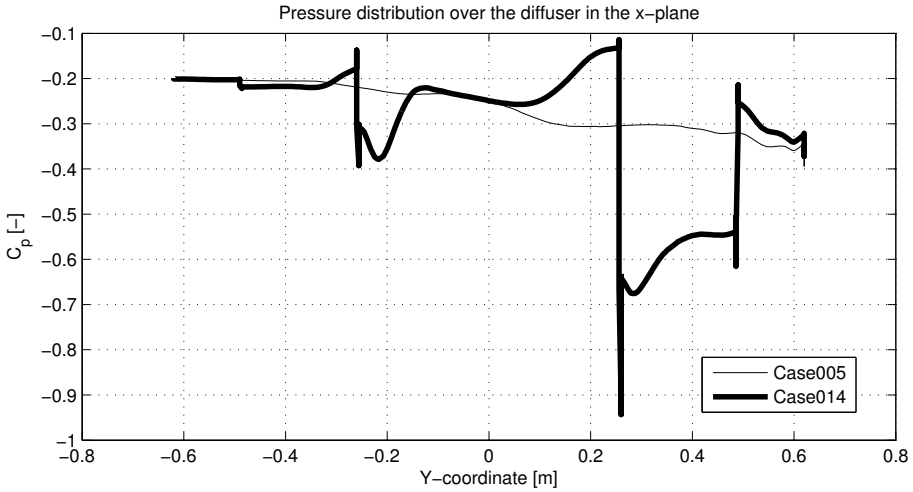

Figure 53: *The pressure distribution over the diffuser in the x-plane during yawed conditions*

However though, the decrease in force is relatively higher in the improved diffuser, see Table 9, whereas the actual obtained downforce is higher than for the original diffuser. It can be said that under these circumstances the improved diffuser is more susceptible to decreasing downforce due to the angle of the oncoming flow. With tuning of the position of the canards it ought to be less sensitive. Still the actual increase in downforce shows that the improved diffuser functions better in both conditions.

4.2.5 Observed trends

There is a complex interaction between the different down force generating devices in the rear. But for this particular configuration and vehicle it can be concluded that the upper wing is not affected by the diffuser. It seems as if the relatively high placement of the upper wing keeps it from affecting the flow underneath the vehicle.

However though, it is a clear trend saying that the devices mounted closer to the body, such as diffuser and lower wing, interact relatively much with eachother. The lower wing influence the upper parts of the base wake whereas the diffuser influence the lower part of the base wake and since the base wake drives the flow through the diffuser there is a clear interaction.

In this particular configuration removing the lower wing has greater effect than improving the diffuser but obviously it is a more radical change to the vehicle and one could not expect anything else.

Unfortunately the goals contradict eachother in that a small base wake is positive when trying to reduce drag whereas it is not as capable of driving the flow through the diffuser.

4.3 Sliding mesh

One of the major drawbacks of running steady CFD-simulations on vehicles with rotating wheels is that the methods used to approximate the wheel rotation into the time-averaged solution are very sensitive as to how the rims are positioned. A difference in orientation of the rim can result in relatively large differences in the predicted flow around the vehicle. A more accurate representation of the wheel rotation is the sliding mesh approach which has been discussed previously in section 2.2 on page 10.

In order to be able to validate the steady results a sliding mesh simulation of the half-domain-baseline configuration was run. A thorough evaluation of half-domain simulations can be found in Appendix D.

Table 10: *A presentation of the cases of interest in this section*

Case009	*Baseline half domain, MRF*
Case020	*Basline half domain, sliding mesh*

It is clearly evident that the steady approach is not able to capture large fluctuations in the flow, the normalised force acting on the diffuser in the x-direction can be seen in Figure 54 and there are substantial fluctuations in the force. The time period in the plot is that of two full revolutions of the wheels and it shows an obvious cyclic behaviour in which it has covered two full cycles during the two revolutions.

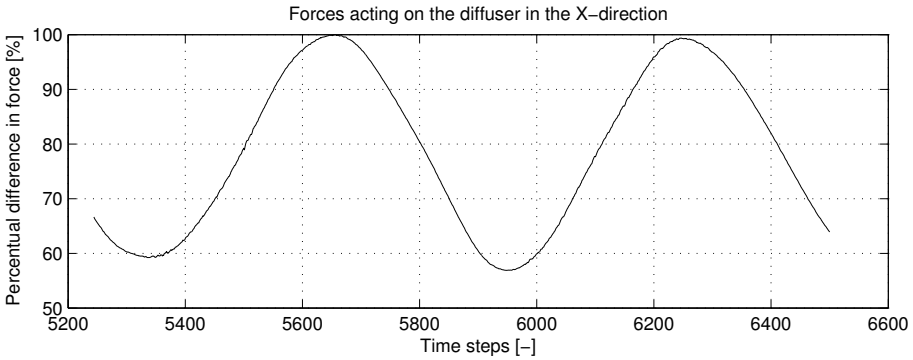

Figure 54: *Force acting on the diffuser in the x-direction, the time period is that of two full revolutions of the wheels.*

Still what needs to be remembered is the fact that the wheels in this configuration are positioned in the same way in both the rear and front, with only a minor speed difference. Usually, due to differences in speed between front and rear wheel due to cornering, differences in diameter etc. the orientation of the rim is bound to be different in the front when compared to the rear and this would of course render a different behaviour. The only conclusion that can be drawn is that there are fluctuations, they seem to have a cyclic behaviour related to a full revolution but they ought to interact in many different ways depending on the orientation of either wheel.

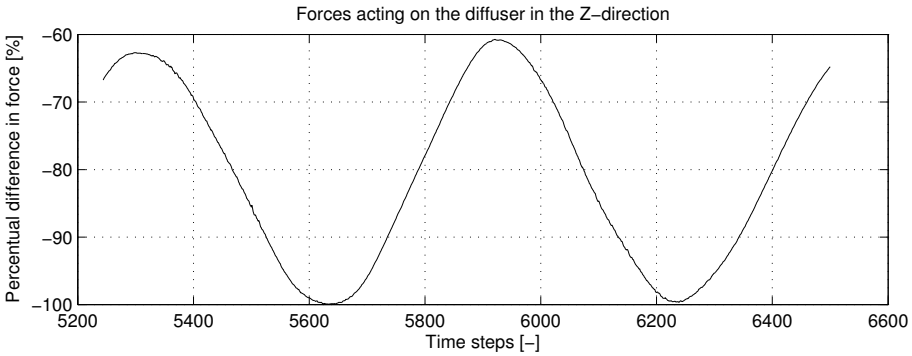

Figure 55: *Forces acting on the diffuser in the z-direction over a time period of two full wheel revolutions*

The fluctuations are mainly evident in the region behind the wheel wakes, such as underbody, diffuser etc. And as can be seen in Figure 55 the effect is just as prominent in the z-direction as in the x-direction.

The interaction between the different parts is hard to analyse due to the irregular conditions under which the vehicle operates, however though, the irregular interactions are somewhat visible in Figure 56, where the total force acting on the vehicle in the z-direction is ploted. It shows the same cyclic behaviour but not in a sinusoidal manor but rather a combination of many other sinusoidal fluctuations.

Figure 56: *The total force acting on the vehicle in the z-direction over a time period of two full wheel revolutions*

Obviously the fluctuations travel through the domain in pretty much the same velocity as the free stream and thus the effect on the different parts have different cycles, this is clearly visible in Figures 57 and 58.

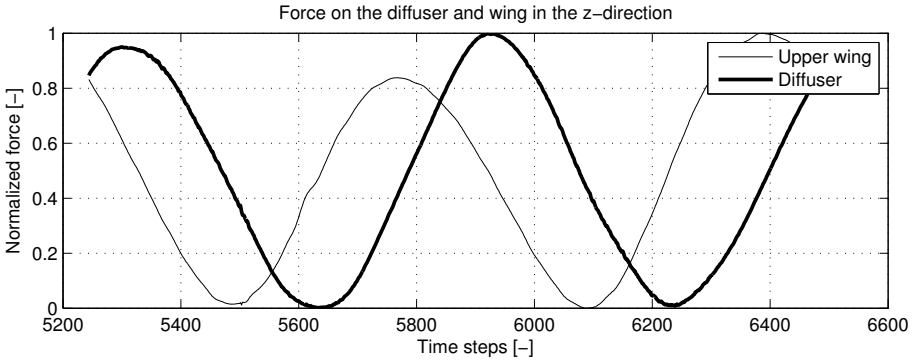

Figure 57: *A comparison of the normalised force, in the z-direction, acting on the upper wing and on the diffuser over a time period of two full wheel revolutions*

Still the actual fluctuations on the upper wing are insignificant when compared to those of the diffuser. One has to keep in mind that the plots in Figures 57 and 58 are normalised in order to enable the evaluation of the cyclic behaviour and not in any way the actual effect on the performance of the vehicle.

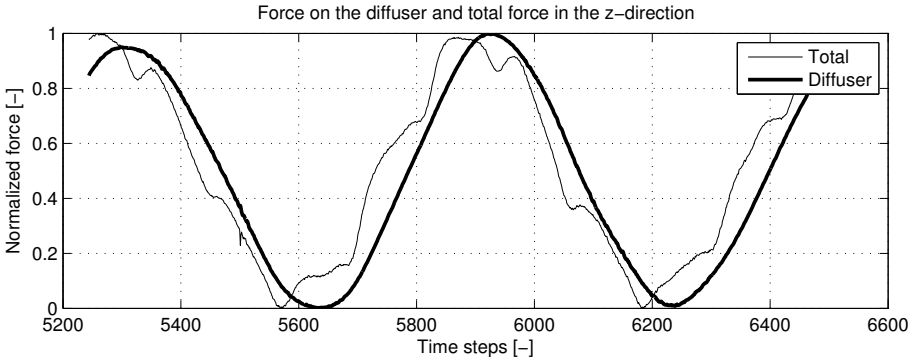

Figure 58: *A comparison of the normalised force, in the z-direction, acting on the vehicle in total and on the diffuser separately over a time period of two full wheel revolutions.*

It can be seen in Figure 59 that there is a significant difference in total pressure, in the diffuser area, at the two extreme operating points. This confirms the difference in lift force at the diffuser between the extreme points. The diffuser area is highlighted.

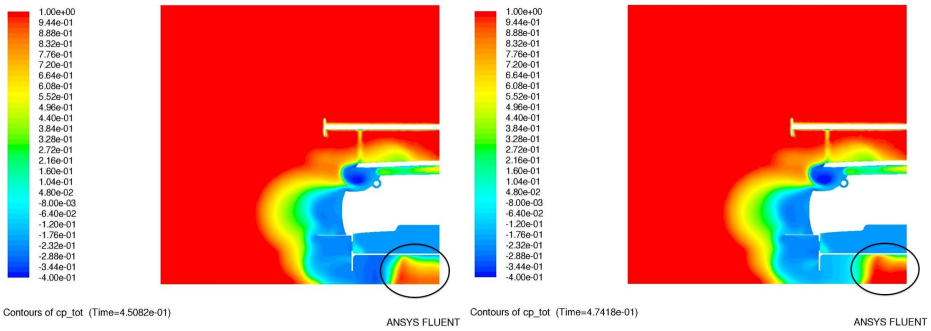

(a) *Time step 5635* (b) *Time step 5927*

Figure 59: *The difference in total pressure coefficient in a x-plane around the wing and diffuser. Figure (a) shows the point where the downforce is at minimum and Figure (b) shows the point of maximum downforce.*

The transient fluctuations are also clearly visible in Figure 60 where a "wave"-like formation is created behind the front wheel. Every vortex shedding is created by passing spokes. Also visible is a large area of low total pressure behind the rear wheel which forms once every wheel revolution and then dissolves into the free stream.

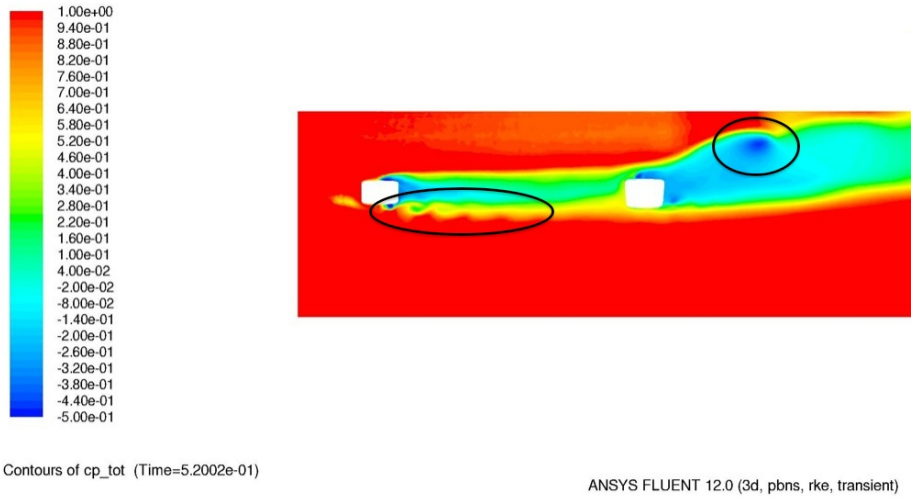

Figure 60: *The coefficient of total pressure in the z-plane showing the transient fluctuations present*

The vortex shedding is highly responsible for the fluctuations in the diffuser.

Even though a lot of details of the flow are left out when using the MRF-approach it is obvious when comparing the lift and drag values in Table 11 on the next page that when time averaging the forces from the sliding mesh simulation there is a good correlation between the two methods, especially for global lift and drag, whereas the moment which yields the lift in the front and rear does not correlate as well.

Table 11: *A comparison of the general drag and lift values between the MRF- and the sliding-mesh approach*

	ΔC_D	ΔC_L	$\Delta C_{L,f}$	$\Delta C_{L,r}$
Case009	-	-	-	-
Case020	0.004	-0.002	0.014	-0.017

4.3.1 Observed trends

A lot of details in the flow are lost when running steady simulations but still the cycles of the fluctuations are so short that in essence there will be no actual difference in predicted performance of the vehicle. However though, it enables the possibility of better being able to understand what happens in the vicinity of the wheels and how it impacts on other aspects of the vehicle.

Still the computational effort needed to run a sliding mesh simulation is so large in comparison with the MRF that unless one is conducting fundamental studies on the effects of rotating wheels, the MRF-approach must be considered as a very good option.

5 Results - Combinations

The results of the combined configurations are presented in the sections below.

5.1 *Case016* Improved diffuser and removed lower wing

This configuration combines the changes implemented in *Case013* and *Case015.* It has previously been concluded that the lower wing and the improved diffuser mainly influence the base wake in the top and the lower part respectively, thus it seems as if most of the positive aspects of the two configurations should be maintained even if combined. The aim of this configuration was thus mainly to reduce the drag by removing the lower wing while maintaining as much downforce as possible with the improved diffuser.

The overall drag and lift values from this configuration are presented as delta values in the Table below.

Table 12: *Delta values compared with Case001*

Case	ΔC_D	ΔC_L	$\Delta C_{L,f}$	$\Delta C_{L,r}$
Case001	-	-	-	-
Case016	-0,034	0,056	0,013	0,044

The effects from the two separate configurations and how they interact is even more clear when looking at figure 55 below. The combined configuration has less drag than both individual configurations and the lift pretty much adds up to the sum of the individual configurations.

The combination result in a downforce balance of 47.6% in the front. Which compared with that of the baseline, which is 45.5% in the front, must be considered well balanced.

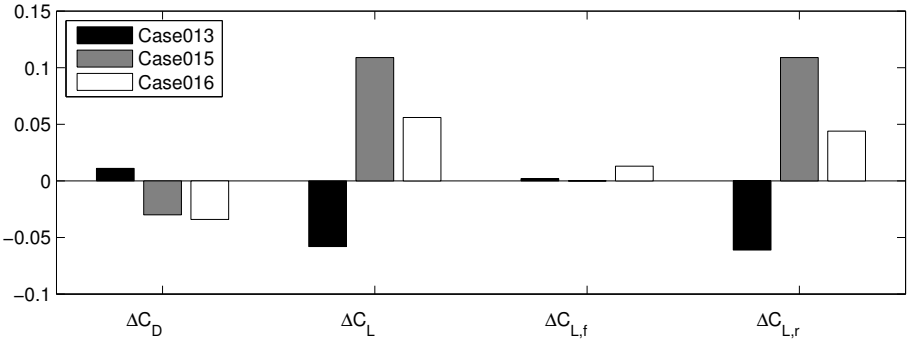

Figure 61: *A bar plot of the delta values of drag and lift for the two separate configurations and the combination.*

By removing the lower wing the total lift of the vehicle increase. However, in this case the improved diffuser is used and hence some of the downforce lost is recovered. The combined effects in this configuration are clearly visible when comparing with the cases where these modifications are implemented individually, see in figure 62 and 63. The areas of interest are highlighted.

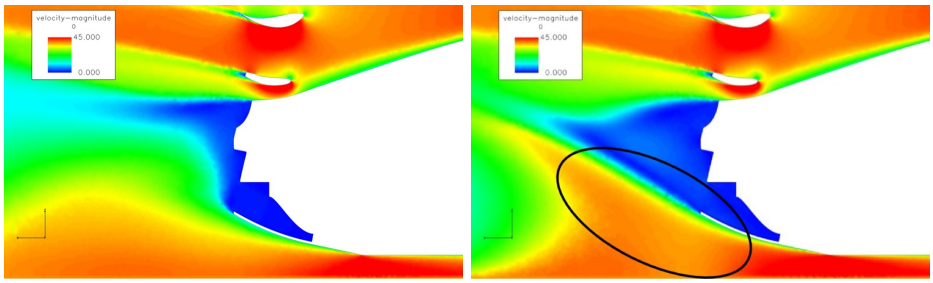

(a) *Case001* (b) *Case013*

Figure 62: *Velocity magnitude, y-plane*

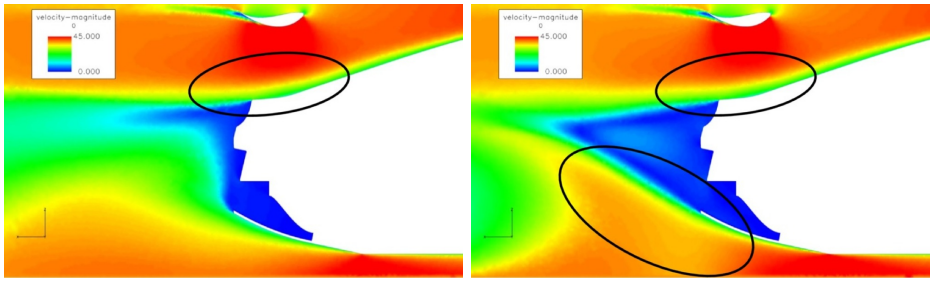

(a) *Case015* (b) *Case016*

Figure 63: *Velocity magnitude, y-plane*

There are obvious similarities between the flow through the diffuser in *Case016* and *Case013* where both are equipped with the improved diffuser with longitudinal canards. Further, the upper part of the base wake structure has similarities with *Case015* where the lower wing was removed.

The combined effect of the configurations is that the base wake is greatly reduced, however though, the diffuser does not experience quite the same driving force due to the higher pressure in the base wake which follows from the removal of the lower wing.

5.2 *Case018* Improved diffuser, removed lower wing, less agressive wing profile and rear wheel covered

This is a configuration where all benefits from different configurations are combined in order to investigate if the improvements achieved individually, are still present when combined. The delta values compared with *Case001* are presented in Table 13.

Table 13: *Delta values compared with Case001*

Case	ΔC_D	ΔC_L	$\Delta C_{L,f}$	$\Delta C_{L,r}$
Case001	-	-	-	-
Case018	-0,021	-0,021	0,010	-0,031

By removing the lower wing a significant decrease in drag is achieved as well as an increase in downforce. By combining this modification with configurations that also has shown a tendency to increase the downforce, the drag can be reduced and the downforce can be increased. However all the downforce generating devices are located at the rear which shifts the lift balance to the rear. This configuration is clearly showing potential in both increasing the downforce and reducing drag but the lift balance is not beneficial. The pressure distribution over the surface of the wing can be compared with *Case017*, where the lower wing is present, in figure 64.

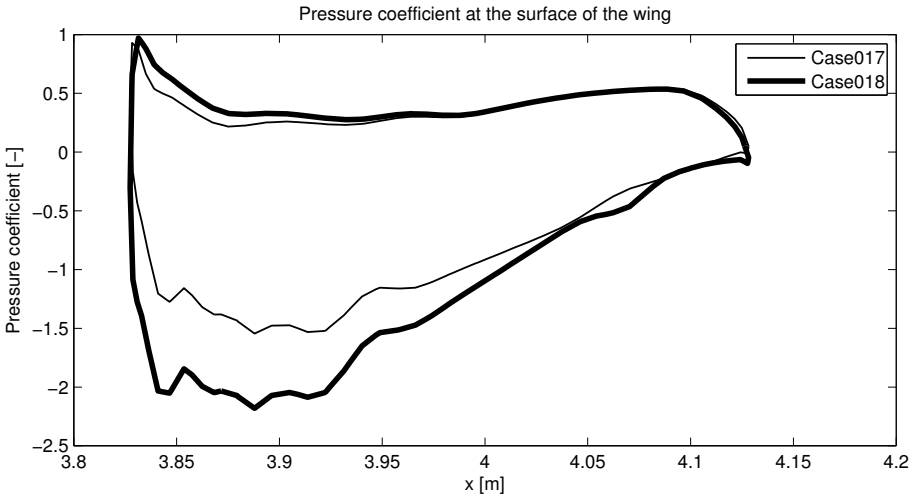

Figure 64: *C_p-distribution at the surface of the wing*

There is a large decrease in pressure underneath the wing compared with *Case017* which gives an increase in downforce generated from the wing. However the body generates more lift without the lower wing as already indicated in *Case015* where the lower wing also was removed. Comparing the forces in x-direction acting on individual parts with other configurations it becomes obvious that removing the lower wing reduce the base wake and hence the aerodynamic drag induced from the body. The drag generated from the diffuser is increased when adding longitudinal canards. However the drag reduction at the diffuser when removing the lower wing and reducing the size of the base wake is also achieved for this case. Hence the percentual increase compared with *Case001* is not as large as for *Case013.* The drag induced from the upper wing shows the same tendency as *Case015,* that a significant reduction is achieved when removing the lower wing.

When it comes to lift forces this configuration seem to follow *Case015,* where the lower wing was removed, with increase in lift generated from the body and windows. Removing the lower wing, or changing to a less agressive profile, seem to individually result in the same magnitude of percentual increase in downforce, compared with *Case001.* In this combined configuration it is indicated that those modifications works together resulting in a significantly higher downforce. The downforce generated from the diffuser is not as high as for *Case013* with only the improved diffuser. This is since the base wake driving the flow through

the diffuser is significanly smaller due to the removal of the lower wing. The wake structure can be compared with *Case001* in figure 65.

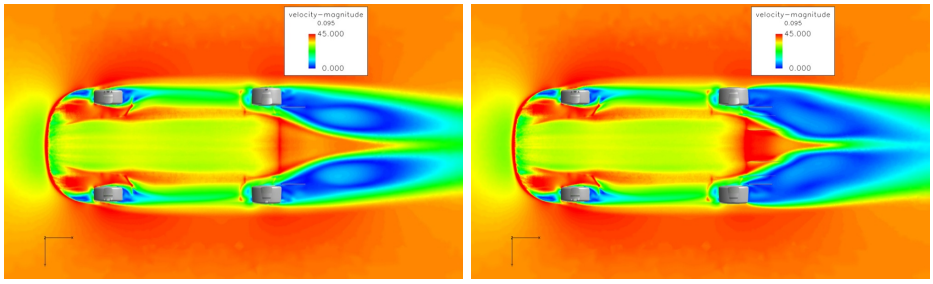

(a) *Case001* (b) *Case018*

Figure 65: *Velocity magnitude underneath the vehicle, z-plane*

The most significant difference is found in the wake structure behind the vehicle starting from the rear wheels. The high velocity regions are more concentrated to the middle section of the diffuser as consequense of the appearence of the longitudinal carnards. There can also be noted a difference at the rear wheels where the wake structure at the outside of the rims is created from the rear of the wheel for this configuration.

By comparing with *Case016,* the influences from the new diffuser and removal of the lower wing, indicated in earlier cases, can be confirmed based on the similarities in figure 66.

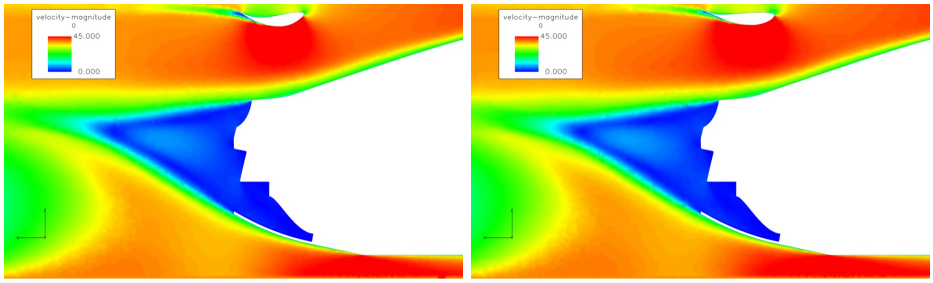

(a) *Case016* (b) *Case018*

Figure 66: *Velocity magnitude, y-plane*

It is clear from the similarities in the above figures that the shape of the base wake, at $y = 0m$, is mainly influenced by the diffuser design and the lower wing. In *Case016* as well as in this case the lower wing is removed and the diffuser is equipped with longitudinal canards.

In the rim design study, a low total pressure area around the contact patch at the rear wheel, can be found in *Case003* exclusively. In this case the front wheel is not covered whilst the rear wheel is covered, as in *Case003.* Figure 67 shows that the low total pressure area also appears for this case.

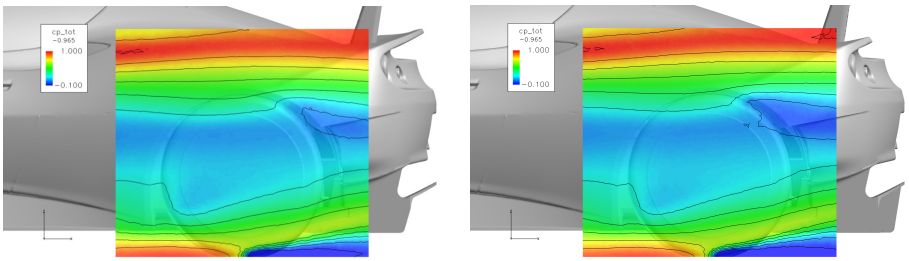

(a) *Case003* (b) *Case018*

Figure 67: $C_{p,tot}$*-distribution around the rear wheel, y-plane*

When comparing the delta values for this case with the other cases it is obvious that this is a good compromise between downforce and reduced drag. It is not the case with the largest drag reduction nor the case with the largest increase in downforce, but it is the only case where a significant reduction in drag and a significant increase in downforce are achieved in the same case. Hence this configuration can be considered as a good compromise between downforce and drag. However, as mentioned before, the lift balance between the front and rear axle is not beneficial.

6 Conclusion

From the results of all the different configurations that has been simulated in this project, a number of trends have been discovered. By studying the similarities or dissimilarities in the flow fields for the different configurations, the influence on the flow field of a certain geometry change, can be determined. If a specific phenomena appears in several cases where the same kind of geometry changes have been implemented, it can be considered likely that the phenomena is related to the geometry change. The conclusions that have been drawn in this study can be condensed to a number of points:

- Covering the front wheel is generally decreasing the drag whilst the lift is increased significantly due to increased static pressure inside the rim and wheel house.
- The flow around the rear wheel is highly dependent on the front wheel geometry.
- Covering the rear wheel does not significantly affect the drag, whereas the downforce is generally increased. A minor increase in downforce, generated from the diffuser, is observed for both cases where the rear wheels are covered. This indicates that the wheel geometry does affect the diffuser flow by maintaining a high velocity magnitude through the diffuser.
- The upper wing is mounted sufficiently high above the body to be of very little influence on the base wake and diffuser.
- An interaction between the lower wing and the diffuser flow is clearly observed. The removal of the lower wing reduce the size of the base wake which to a great extent drives the flow through the diffuser.
- The removal of the lower wing increase the downforce from the upper wing which highlights the importance of undisturbed flow around the wing. Furthermore, the simulations of the wing configurations showed the need for optimisation of the wing profile and angle of attack.
- The diffuser benefits from undisturbed flow at the underbody and canards that maintains the velocity in the diffuser rather than letting the rear wheel wakes propagate into the diffuser.
- Regarding the modelling aspects it can be concluded that the lift is less well predicted, for spoked rims, by the moving wall boundary condition than for the MRF or sliding mesh due to the fact that less turbulence and crossflow is induced by the rims and thereby velocity is increased underneath the vehicle and in the diffuser.

However, these conclusions can only be considered valid for this specific vehicle, allthough it could be an indication that the same phenomenas might be found for a similar kind of vehicle. Further investigations are needed to confirm these conclusions.

7 Recommendations

As mentioned earlier, full domain with wheel rotation modeled by MRF and half domain with sliding mesh showed good correlation. However to confirm the trends that has been found in this project thoroughly, further investigations is needed. To validate the numeric result an asymptotic solution should be achieved. That means that the same case should be simulated using computational grids of different sizes, different turbulence models e.g. $k-\omega$ or *Reynolds Stress model* and different wall functions e.g. *near-wall model approach.* If the solutions are generating the same result it could be considered an asymptotic solution.

It could also be interesting to use time dependent solving methods e.g. *LES* that better predicts the turbulence and include eddies in a wider spectrum of sizes. Furthermore, using other solving methods could validate how good *RANS* with *realizable* $k-\varepsilon$ predicts separation points. However due to time limitations, all kinds of method validations have been excluded from this project.

Furthermore a detailed study e.g. only including one wheel and a wheel house or only including a wing or diffuser, could also be useful in order to understand the different phenomenas in external vehicle aerodynamics of a racecar. By only focusing on a specific detail a computational grid with higher resolution could be used as well as a more computational demanding solving method.

References

[1] Barnard RH. Road Vehicle Aerodynamic Design - An Introduction. 2nd ed. MechAero Publishing; 2001.

[2] Mercker E, Breuer N, Berneburg H, Emmelmann HJ. On the Aerodynamic Interference due to Rolling Wheels of Passenger Cars. SAE Technical Paper Series. 1991;910311.

[3] Dimitrou I, Klussmann S. Aerodynamic Forces of Exposed and Enclosed Rotating Wheels as an Example of the Synergy in the Development of Racing and Passenger Cars. SAE Technical Paper Series. 2006;2006010805.

[4] Zhiling Q. Wheel Aerodynamic Developments by Module-Based Prototype Rims and Stationary Rim Shields. Department of Applied Mechanics, Chalmers University of Technology; 2009.

[5] Fackrell JE, Harvey JK. The Flow Field Pressure Distribution of an Isolated Road Wheel. Advances in Road Vehicle Aerodynamics. 1973;Paper 10.

[6] Fackrell JE, Harvey JK. The Aerodynamics of an Isolated Road Wheel. Aerodynamics of Sports and Competition Automobiles. 1974;Vol. 16.

[7] Axon L, Garry K, Howell J. The Influence of Ground Condition on the Flow Around a Wheel Located Within a Wheelhouse Cavity. SAE Technical Paper Series. 1999;1999010806.

[8] Mears AP, Dominy RG. Racing Car Wheel Aerodynamics - Comparisons Between Experimental and CFD Derived Flow-Field Data. SAE Technical Paper Series. 2004;2004-01-3555.

[9] McManus J, Zhang X. A Computational Study of the Flow Around an Isolated Wheel in Contact With the Ground. Journal of Fluids Engineering. 2006;Vol. 128.

[10] Mlinaric P. Investigations of the Influence of Tyre Deformation and Tyre Contact Patch on CFD Predictions of Aerodynamic Forces on a Passenger Car. Department of Applied Mechanics, Chalmers University of Technology; 2007.

[11] Landström C. Flow Field Investigations of Rotating Wheels on Passenger Cars. Department of Applied Mechanics, Chalmers University of Technology; 2009.

[12] Versteeg HK, Malalasekera W. An Introduction to Computational Fluid Dynamics - The Finite Volume Method. 2nd ed. Pearson Education Limited; 2007.

[13] White FM. Fluid Mehanics. 6th ed. McGraw-Hill; 2008.

[14] Davidsson L. Numerical Methods for Turbulent Flow. Chalmers University of Technology, Department of Applied Mechanics; 2009.

[15] ANSYS Fluent 12.0 Theory Guide; 2009.

[16] ANSYS Fluent 12.0 User's Guide; 2009.

[17] Davidsson L. An Introduction to Turbulence Models. Chalmers University of Technology, Department of Thermo and Fluid Dynamics; 2003.

Appendix

A Case descriptions

The complete list of cases that have been carried out can be found in Table i.

Table i: *Case descriptions*

Simulation name	Description	5° yaw	Half domain
Case001	Baseline		
Case002	Front wheel covered		
Case003	Rear wheel covered		
Case004	Both front and rear wheel covered		
Case005	*Case001* yawed at 5*deg*	X	
Case006	*Case002* yawed at 5*deg*	X	
Case007	*Case003* yawed at 5*deg*	X	
Case008	*Case004* yawed at 5*deg*	X	
Case009	*Case001* Half domain		X
Case010	*Case002* Half domain		X
Case011	*Case003* Half domain		X
Case012	*Case004* Half domain		X
Case013	Improved diffuser design		
Case014	*Case013* yawed at 5*deg*	X	
Case015	Removed lower wing		
Case016	Improved diffuser and removed lower wing		
Case017	Upper wing replaced with less agressive wing profile		
Case018	Improved diffuser, removed lower wing, less agressive wing profile and rear wheel covered		
Case019	*Case001* Moving wall		
Case020	*Case001* Sliding mesh		X

B Standard coordinate planes

In order to compare the different configurations a number of standard planes are defined. One y-plane and one x-plane are defined by each wheel. The y-planes are positioned $30mm$ outside of the vehicle and symmetric around the wheel center in x-direction. The x-plane is positioned $500mm$ downstream from the wheel center. The dimensions of the planes can be found in the Figure below.

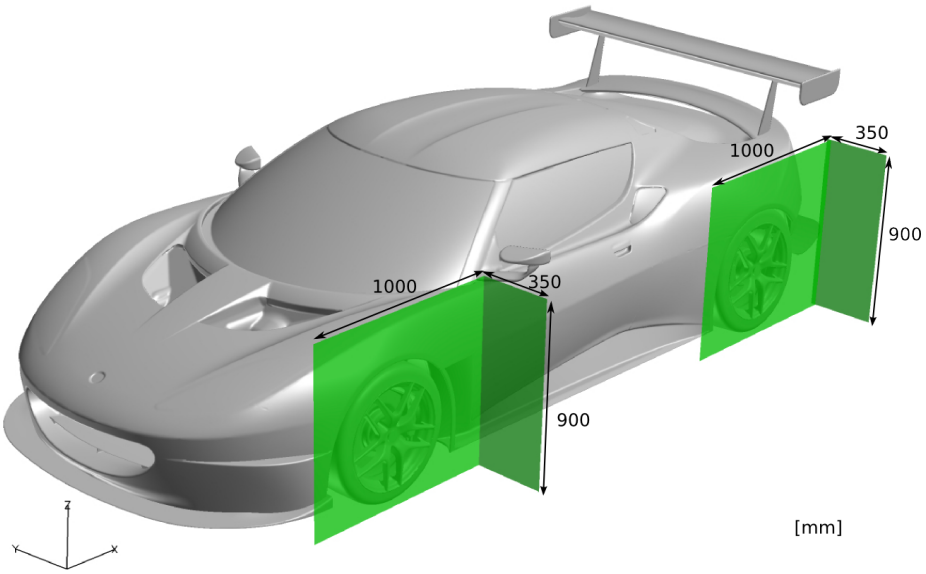

Figure i: *Standard y-plane and x-plane by the front and rear wheel*

The flow underneath the vehicle is often visulised in a z-plane positioned $95mm$ above ground. This is $5mm$ under the vehicle. This plane can be found in the Figure below.

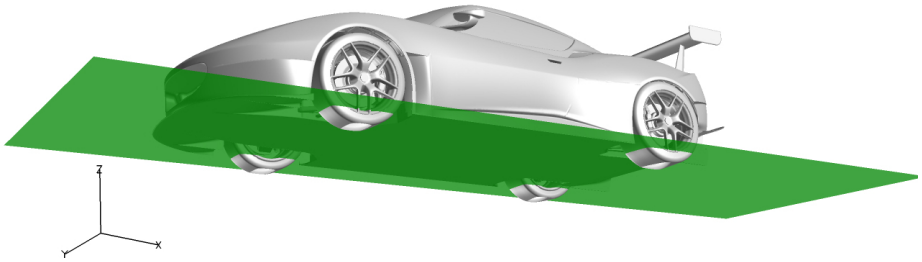

Figure ii: *Plane defined at* $z = 0.095m$

Another plane is defined at $y = 0m$, in the middle of the vehicle. This y-plane can be found in the Figure below.

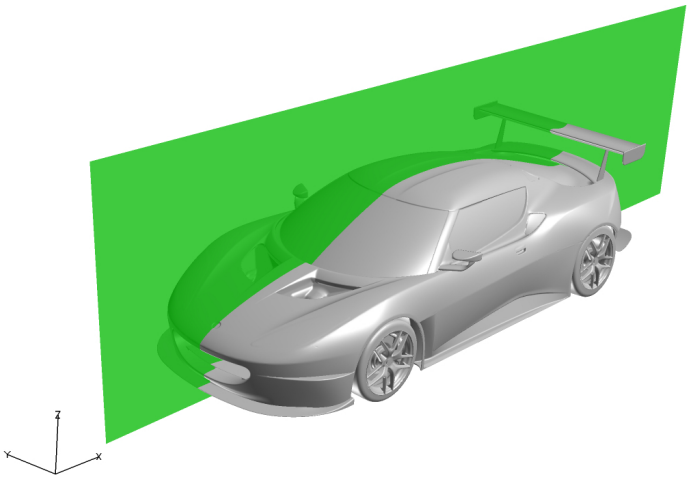

Figure iii: *Plane defined at* $y = 0m$

An x-plane is defined at $x = 4m$, at the rear of the vehicle, to display the flow around the wing and diffuser. This plane can be found in the Figure below.

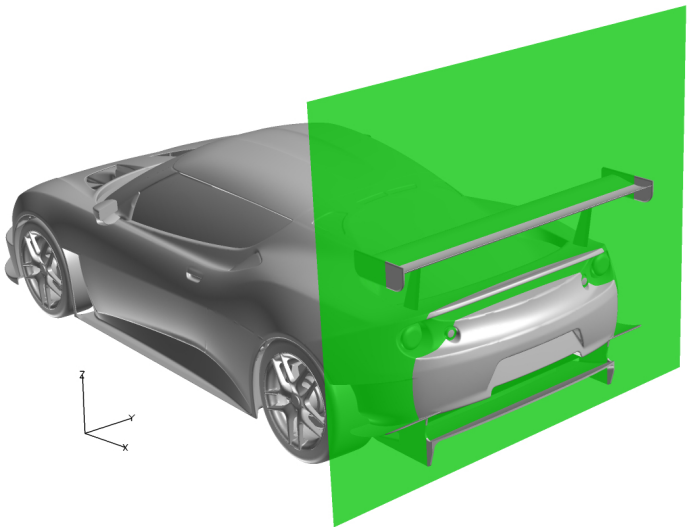

Figure iv: *Plane defined at* $x = 4m$

C MRF and Moving wall comparison

The baseline geometry with these different boundary and cell zone conditions showed a significant difference as expected. The delta values when switching from MRF to moving wall are presented in the Table below.

Table ii: *Delta values for drag and lift when moving wall is compared with MRF*

Case	ΔC_D	ΔC_L	$\Delta C_{L,f}$	$\Delta C_{L,r}$
Case001	-	-	-	-
Case019	-0,001	-0,023	-0,010	-0,013

From the Table above it is obvious that the drag force can be predicted quite well with the moving wall boundary condition. However, the lift force differs quite a lot. The significant increase in downforce for each wheel axle seems to be in the same magnitude.

The total pressure coefficients around the wheels for the baseline configuration can be studied in the Figure below.

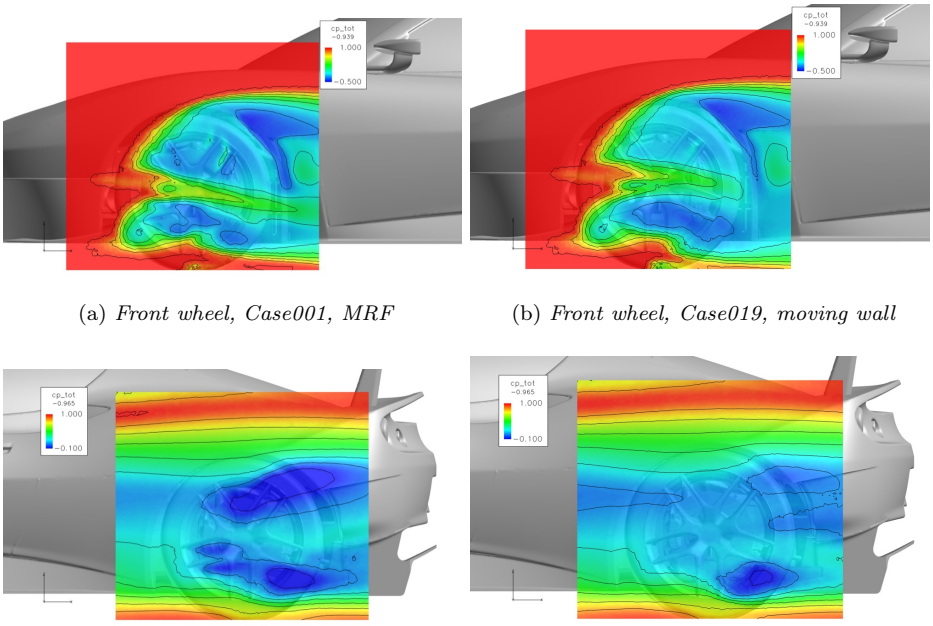

(a) *Front wheel, Case001, MRF*

(b) *Front wheel, Case019, moving wall*

(c) *Rear wheel, Case001, MRF*

(d) *Rear wheel, Case019, moving wall*

Figure v: $C_{p,tot}$ *distribution around the wheels, y-plane*

In these Figures a significant difference can be noted between the MRF and the moving wall configurations. The fact that the fluid inside the rims of the moving wall configuration is not actually modelled as moving shows a substantial influence on the total pressure distribution around the wheel. The flow field in the vicinity of the rims is significantly less influenced by pressure gradients for

the moving wall configuration. In the Figure below the total pressure coefficient distribution is displayed in a x-plane instead.

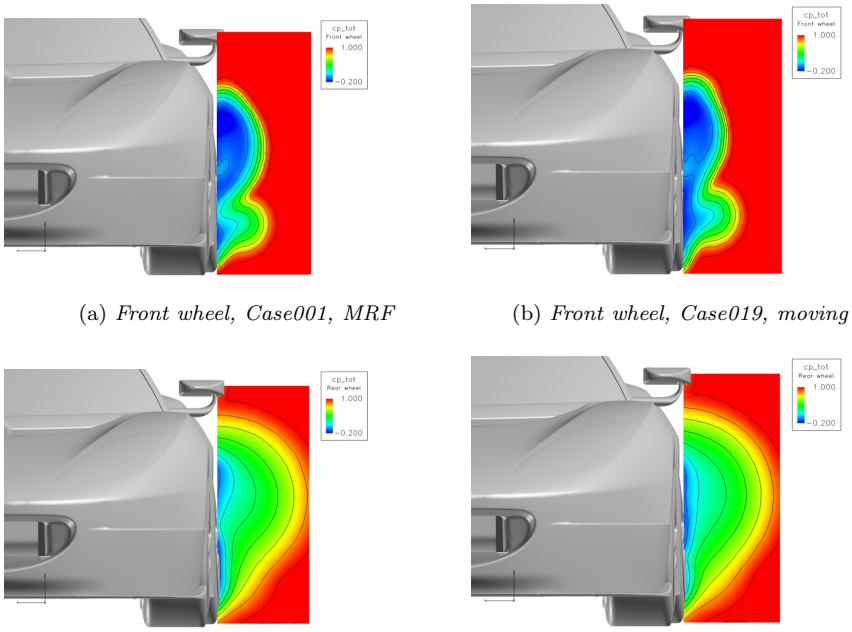

(a) *Front wheel, Case001, MRF*

(b) *Front wheel, Case019, moving wall*

(c) *Rear wheel, Case001, MRF*

(d) *Rear wheel, Case019, moving wall*

Figure vi: $C_{p,tot}$ *distribution around the wheels, x-plane*

Also in this view a substantial difference in total pressure distribution between the configurations. Especially the difference in size of the low total pressure region behind the front wheel can be noted.

An interesting phenomena is that most of the increase in downforce comes from the underbody which again shows the importance of not disturbing the flow underneath the vehicle. Since the moving wall configuration does not induce as much turbulence from the rims as for the MRF configuration, the flow under the vehicle and through the diffuser is less disturbed, hence the increase in downforce from the underbody.

The moving wall boundary condition seem to give a good approximation for the global drag force, whereas for the local flowfield and the lift forces a more realistic method is needed in order to get an accurate result.

D Half and full domain comparison

The geometry used in the simulations is almost symmetric allthough some differences between the two halves can be found. The cooling duct for example is not symmetric and hence an unsymmetric flow can be achieved. Therefore the most accurate way of simulating the configurations is to use a full domain with a complete, full sized vehicle.

In order to model the wheel motion properly including the pumping effect from the spokes, a transient simulation with sliding mesh is needed. Hence the computation time is heavily increased. To reduce the time, the transient simulation was performed on a half domain with much lower resolution than for the steady simulations. To evaluate the use of a half domain the covered wheel configurations were also performed on half domain.

However, the transient simulation can cause fluctuations in the basewake that makes the simulation unsymmetric. Allthough the result of a transient full domain is dependent of the position of the spokes relative to the corresponding wheel at the other side of the vehicle.

The results of the half domain simulations showed a good correlation with the full domain simualations. The drag and lift values for the half domain cases compared with the full domain can be found as delta values in the Table below.

Table iii: *Delta values between half and full domain for each configuration*

Case	ΔC_D	ΔC_L	$\Delta C_{L,f}$	$\Delta C_{L,r}$
Case001	-	-	-	-
Case009	0,006	0,007	0,017	-0,010
Case010	0,001	-0,000	0,008	-0,009
Case011	0,004	0,019	0,021	-0,002
Case012	-0,001	-0,004	0,005	-0,009

The delta values are all in the magnitude of a number of counts except when the front wheel is not covered resulting in an increase in lift in the front of the vehicle for the half domain simulation. This could be due to the difference in resolution, or an effect of that the unsymmetry of the cooling duct is not represented. When the front wheel is not covered the flow through the brake cooling ducts is increased. Since the intakes for the brake cooling ducts is located inside the main cooling duct the influence from the unsymmetry could be larger when the front rims are not covered. However, the downforce at the rear axle seems to increase for all configurations when using half domain.

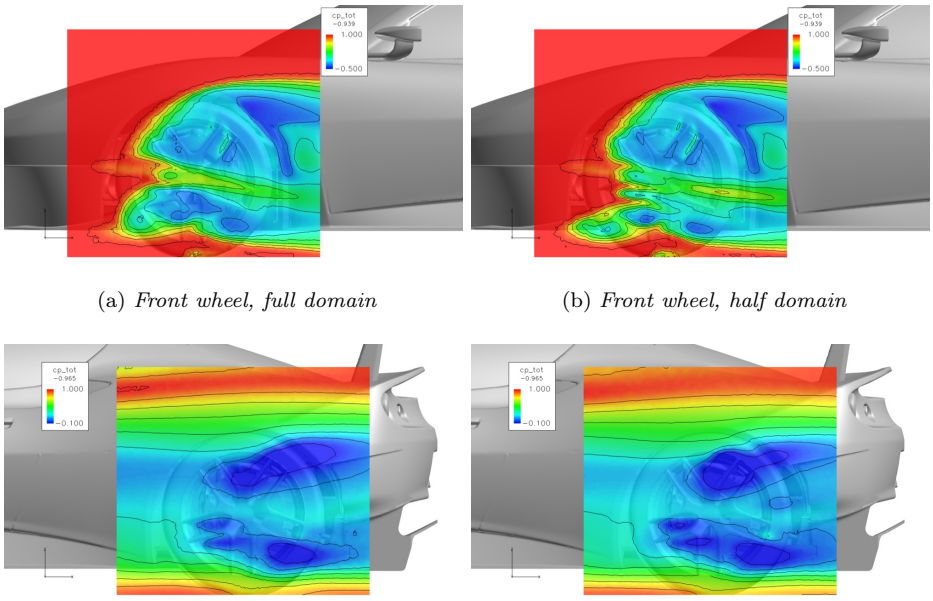

(a) *Front wheel, full domain*

(b) *Front wheel, half domain*

(c) *Rear wheel, full domain*

(d) *Rear wheel, half domain*

Figure vii: *Baseline, C_p around the wheels, y-plane*

There is a slight difference in flow pattern around the front wheel in this configuration. In the front of the wheel there is a larger area of high total pressure.

The pressure around the wheels for the configuration where only the front wheel was covered can be seen, for both full and half domain, in the Figure below.

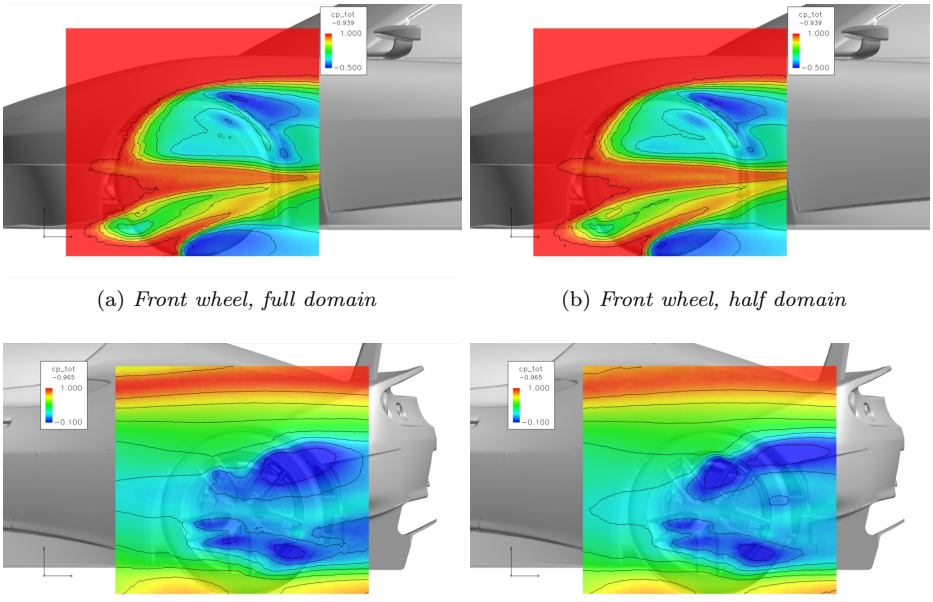

(a) *Front wheel, full domain*

(b) *Front wheel, half domain*

(c) *Rear wheel, full domain*

(d) *Rear wheel, half domain*

Figure viii: *Front wheel covered, C_p around the wheels, y-plane*

Also in this Figure the different cases shows outstanding similarities between full and half domain. However, some minor differences can be seen. The drag and lift values shows only minor differences aswell.

In the Figure below, the total pressure around the front and rear wheel, for the configuration where the rear wheel is covered, for both full and half domain can be compared.

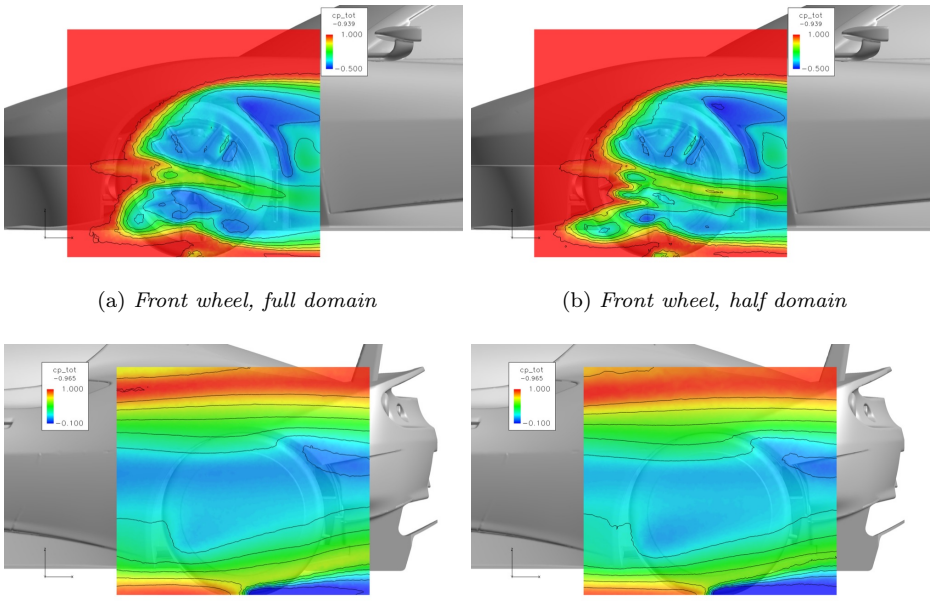

(a) *Front wheel, full domain*

(b) *Front wheel, half domain*

(c) *Rear wheel, full domain*

(d) *Rear wheel, half domain*

Figure ix: *Rear wheel covered, C_p around the wheels, y-plane*

The same phenomena as for the baseline configuration is found for the front wheel in this configuration as well. The lift force increase for the front axle from full domain to half domain is in the same magnitude as for the baseline configuration as well. Hence the largest difference between full and half domain seems to be located around the front wheel when the front rim is not covered as the lift values in Table iii indicated.

In the Figure below the pressure around the front and rear wheel can be compared between the full and half domain for the configuration where both front and rear wheel were covered. However

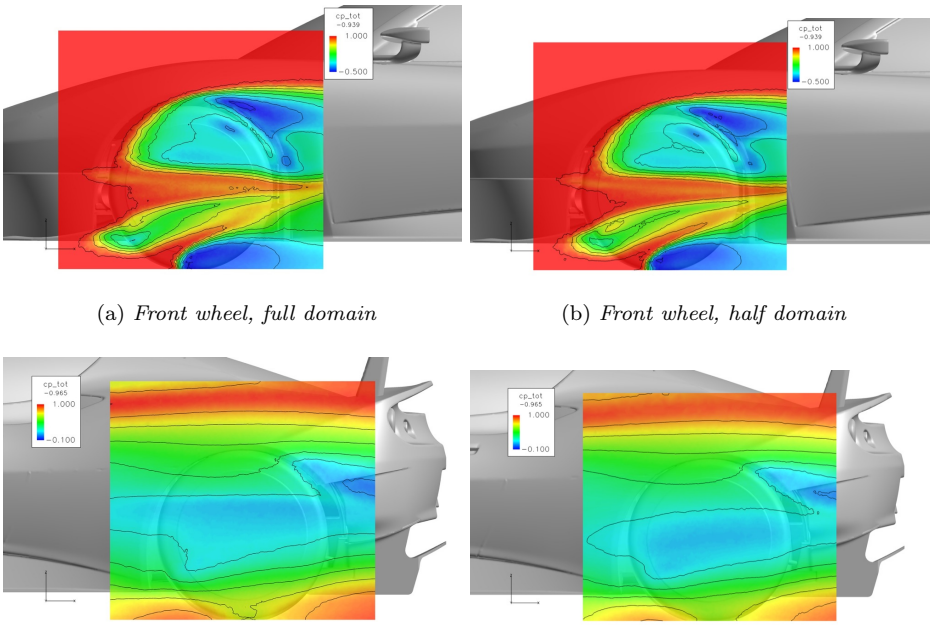

(a) *Front wheel, full domain*

(b) *Front wheel, half domain*

(c) *Rear wheel, full domain*

(d) *Rear wheel, half domain*

Figure x: *Both wheels covered, C_p around the wheels, y-plane*

Also this configuration shows good correlation with full domain around the wheels, since the Figures are almost identical. However, this configuration did not show much differences between full and half domain in terms of forces either. The flow passing the front of the wheel shows a slightly different pattern.

In general it could be stated that a half domain gives a fairly good result though some phenomenas are not accounted for.